

A New Pansharpening Method Based on Spatial and Spectral Sparsity Priors

Xiyan He, Laurent Condat, José M. Bioucas-Dias, *Member, IEEE*, Jocelyn Chanussot, *Fellow, IEEE*, and Junshi Xia, *Student Member, IEEE*

Abstract—The development of multisensor systems in recent years has led to great increase in the amount of available remote sensing data. Image fusion techniques aim at inferring high quality images of a given area from degraded versions of the same area obtained by multiple sensors. This paper focuses on pansharpening, which is the inference of a high spatial resolution multispectral image from two degraded versions with complementary spectral and spatial resolution characteristics: 1) a low spatial resolution multispectral image and 2) a high spatial resolution panchromatic image. We introduce a new variational model based on spatial and spectral sparsity priors for the fusion. In the spectral domain, we encourage low-rank structure, whereas in the spatial domain, we promote sparsity on the local differences. Given the fact that both panchromatic and multispectral images are integrations of the underlying continuous spectra using different channel responses, we propose to exploit appropriate regularizations based on both spatial and spectral links between panchromatic and fused multispectral images. A weighted version of the vector total variation norm of the data matrix is employed to align the spatial information of the fused image with that of the panchromatic image. With regard to spectral information, two different types of regularization are proposed to promote a soft constraint on the linear dependence between the panchromatic and fused multispectral images. The first one estimates directly the linear coefficients from the observed panchromatic and low-resolution multispectral images by linear regression while the second one employs the principal component pursuit to obtain a robust recovery of the underlying low-rank structure. We also show that the two regularizers are strongly related. The basic idea of both regularizers is that the

Manuscript received January 6, 2014; revised April 18, 2014; accepted June 11, 2014. Date of publication June 27, 2014; date of current version August 21, 2014. This work was supported in part by the Hypanema Project through the Agence Nationale de la Recherche under Grant ANR-12-BS03-0003 and in part by the Portuguese Science and Technology Foundation under Project PEst-OE/EEI/LA0008/2013 and Project PTDC/EEI-PRO/1470/2012. The associate editor coordinating the review of this manuscript and approving it for publication was Prof. Farhan A. Baqai.

X. He, L. Condat, and J. Xia are with the GIPSA-Laboratory, University of Grenoble, Grenoble F-38402, France (e-mail: greenhxy@gmail.com; laurent.condat@gipsa-lab.grenoble-inp.fr; junshi.xia@gipsa-lab.grenoble-inp.fr).

J. M. Bioucas-Dias is with the Instituto de Telecomunicações, Instituto Superior Técnico, Universidade de Lisboa, Lisbon 1649-004, Portugal (e-mail: bioucas@lx.it.pt).

J. Chanussot is with the GIPSA-Laboratory, University of Grenoble, Grenoble F-38402, France, and also with the Faculty of Electrical and Computer Engineering, University of Iceland, Reykjavik 101, Iceland (e-mail: jocelyn.chanussot@gipsa-lab.grenoble-inp.fr).

This paper has supplementary downloadable material available at <http://ieeexplore.ieee.org>, provided by the author. The supplementary material contains the details of the parameter selection and the algorithm performance of the two proposed methods. It can also be downloaded at <http://www.gipsa-lab.fr/~jocelyn.chanussot/SupplementaryMaterial.pdf>. The total size of the file is 82.5 kB. Contact greenhxy@gmail.com for further questions about this work.

Color versions of one or more of the figures in this paper are available online at <http://ieeexplore.ieee.org>.

Digital Object Identifier 10.1109/TIP.2014.2333661

fused image should have low-rank and preserve edge locations. We use a variation of the recently proposed split augmented Lagrangian shrinkage algorithm to effectively solve the proposed variational formulations. Experimental results on simulated and real remote sensing images show the effectiveness of the proposed pansharpening method compared with the state-of-the-art.

Index Terms—Image fusion, pansharpening, remote sensing, principal component pursuit, total variation, low rank recovery, convex optimization, proximal splitting method, split augmented Lagrangian shrinkage (SALSA).

I. INTRODUCTION

NOWADAYS multisensor systems are widely used in many fields such as remote sensing, medical imaging and computer vision. The increasing availability of different data sources from the same phenomenon, object, or area, often with complementary characteristics, has stimulated research in data fusion aimed at producing better inferences about the phenomenon, object, or area under study. In general, image fusion combines information of multiple images with the purpose of providing significant advantages over single source image, such as improved system reliability or classification accuracy [1], [2]. In the context of remote sensing, pansharpening is a type of image fusion which has become a hot research topic for the enhancement of the image spatial resolution [3]–[10]. High quality remote sensed images are valuable for many applications, such as environmental monitoring, natural resources locating, or weather and natural disaster forecasting. Remote sensing systems rely primarily on spaceborne imaging sensors, which provide panchromatic (Pan) and multispectral (MS) images with different characteristics. A Pan image contains only one band of reflectance data that covers a broad spectral range. This allows smaller detectors to be used while maintaining a high signal-to-noise ratio. Therefore, a Pan image has generally low spectral resolution but high spatial resolution. By contrast, an MS image contains more than one band. The spectral range of each band of an MS image is less than that of the Pan image, resulting in high spectral resolution but low spatial resolution. It is beneficial to combine the complementary information of Pan and MS images, so as to generate a color image of both high spectral and high spatial resolutions, using pansharpening techniques. Qualitative advantages of pansharpening for remote sensing systems have been demonstrated in many papers, e.g. for improving the accuracy of snow map detection [11], change detection [12] and classification [2].

A large number of pansharpening techniques has been proposed over the last years [13]. The most commonly used procedures among the remote sensing community are

component substitution methods, because of their fast implementation [14]–[16]. These methods first project the upsampled MS images into a new space. The assumption is that one component of this new representation contains equivalent structures to those of the Pan image. The fusion occurs then with a total or partial substitution of these structures by those of the Pan image. Finally, an inverse projection is performed to obtain the high resolution pansharpened image. Examples of component substitution methods include Intensity-Hue-Saturation (IHS) methods [17], Principal Component Analysis (PCA) [14], [16] and Gram–Schmidt (GS) based method [15]. However, this kind of methods often suffers from the induced spectral distortion, due to the fact that the Pan image does not cover exactly the same wavelengths as the MS image [3]. Several spectral adjustment schemes have therefore been proposed, aiming at improving the spectral quality of the fused image [18]–[20].

Compared to the component substitution methods, multiresolution-analysis methods [21]–[23] have been proposed, with the objective of preserving better spectral characteristics in the high resolution fused image. These methods rely on the injection of the high frequency information of the Pan image into the upscaled MS image. Spatial filters, such as the Discrete Wavelet Transforms (DWT) are often employed to extract the high spatial frequency information from the Pan image [24]–[27]. In contrast to component substitution methods, multiresolution-analysis methods often experience spatial distortions, like ringing or stair-casing effects.

Like many other ill-posed problems in imaging, it is possible to regularize the inverse problem of pansharpening by injecting in the formulation some prior knowledge about the sought-after solution. This way, the problem is transformed into a well-posed convex optimization problem. Typically, consistency with the available data and low energy or sparsity of the solution in some representation is enforced. Within this paradigm, we can mention the P+XS pansharpening method of Ballester *et al.* [28], based on two assumptions. The first is that the Pan image can be approximated as a linear combination of the high resolution multispectral bands. The second is that the geometry information of the spectral channels of an MS image is contained in the topographic map of the corresponding Pan image. One drawback of the P+XS method is that the first assumption is not realistic and may lead to some severe spectral distortion [3]. Therefore, Möller *et al.* [29] proposed to combine the ideas of wavelet based fusion and P+XS method in order to obtain higher spectral quality, while preserving the geometry information of the Pan image.

Departing from these methods, we present in this paper two new regularized formulations of pansharpening, without the aforementioned assumptions. By analyzing the spatial and spectral relationship between the available low-resolution MS image and high-resolution Pan image on one hand, and the unknown high-resolution MS image to estimate on the other hand, we shed light on the sparsity patterns expected in the solution: a spectral low-rank property and a spatial alignment of the geometric structures across the bands. The two proposed formulations based on Linear Regression (LR) or Principal Component Pursuit (PCP) are two different ways of

mathematically expressing the low-rank spectra sparsity prior. In both cases, a variant of the Total Variation (TV) seminorm is introduced and used for spatial regularization, enforcing sparsity in the differences between adjacent pixels.

The paper is organized as follows. In Section II, we formulate the inverse problem of pansharpening and we give a brief description of two methods of the literature to solve it. This is followed by the presentation of our regularized formulation in Section III. The proposed algorithm, called PanSALSA and based on the Split Augmented Lagrangian Shrinkage (SALSA) methodology, is introduced in Section IV. Then, in Section V, we evaluate the proposed method and compare its performance with classical pansharpening methods.

II. FORMULATION OF THE PANSHARPENING INFERENCE PROBLEM AND RELATED WORK

First, let us introduce some notations. Multivalued quantities, like vectors, matrices and images, are denoted by bold letters. Unless otherwise stated, all vectors are arranged into columns. We denote by \mathbf{I} and $\mathbf{0}$ the identity matrix and the zero matrix, respectively, and their dimensions, when not explicitly given, shall be inferred from the context. The symbols $(\cdot)^T$ and $(\cdot)^H$ stand for the transpose and Hermitian (i.e., transpose conjugate) operations, respectively. Let $\mathbf{v}_l \in \mathbb{R}^N$, for $l = 1, \dots, L$ and $N = N_1 N_2$, denote the L original high spatial resolution multispectral image bands of size $N_1 \times N_2$, to be estimated from a) the panchromatic image $\mathbf{p} \in \mathbb{R}^N$ of same size $N_1 \times N_2$ and b) the low-resolution multispectral image bands $\mathbf{u}_l \in \mathbb{R}^M$ of size $(N_1/S) \times (N_2/S)$, for $l = 1, \dots, L$, where $M = N/S^2$ and the downsampling factor $S \geq 1$ is supposed an integer. The images \mathbf{u}_l are degraded (i.e., blurred, downsampled and noisy) versions of \mathbf{v}_l . Given a sequence of vectors $\mathbf{x}_l \in \mathbb{R}^N$, for $l = 1, \dots, L$, usually representing image bands, let $\mathbf{x} = \text{vec}([\mathbf{x}_1, \mathbf{x}_2, \dots, \mathbf{x}_L]) \in \mathbb{R}^{NL}$ and $\text{vec}^{-1}(\mathbf{x}) = [\mathbf{x}_1, \mathbf{x}_2, \dots, \mathbf{x}_L]$ stand for the columnwise stacking and unstacking operations, respectively. Given $\mathbf{n} = (n_1, n_2) \in \Omega$, where $\Omega = \{1, \dots, N_1\} \times \{1, \dots, N_2\}$ is the image domain, $\mathbf{x}_i[\mathbf{n}]$ denotes the pixel value of \mathbf{x}_i at location \mathbf{n} and $\mathbf{x}[\mathbf{n}] = [\mathbf{x}_1[\mathbf{n}], \dots, \mathbf{x}_L[\mathbf{n}]]^T$.

Introducing $\mathbf{v} = \text{vec}([\mathbf{v}_1, \mathbf{v}_2, \dots, \mathbf{v}_L])$ and $\mathbf{u} = \text{vec}([\mathbf{u}_1, \mathbf{u}_2, \dots, \mathbf{u}_L])$, we are in position to formulate the observation model, like in [30], as

$$\mathbf{u} = \mathcal{R}\mathbf{v} + \mathbf{w}, \quad (1)$$

where $\mathcal{R} : \mathbb{R}^{NL} \mapsto \mathbb{R}^{ML}$ is the linear operator modeling blurring and downsampling by a factor of S taking place at the sensor and \mathbf{w} is a vector of i.i.d. noise with zero mean. \mathcal{R} maps a multispectral image of size $N_1 \times N_2$ to a multispectral image of size $(N_1/S) \times (N_2/S)$, with same number of bands, in their stacked form. The estimation of \mathbf{v} based on the observation model (1) is obviously an ill-posed problem, mainly due to loss of information in the downsampling process. Thus, it is necessary to regularize the problem, by introducing penalties that promote solutions with desirable properties. This turns the estimation problem into an optimization problem, which consists in minimizing an objective function containing data terms, accounting for the consistency with the available data,

and regularization terms, favoring desirable properties in the solution image.

The total variation (TV) seminorm [31]–[33] is an effective regularizer for inverse problems. In particular, TV based methods have achieved great success in many image processing applications, like restoration, denoising, or inpainting [34]. Generally, for a scalar image z with domain Ω , the TV seminorm is defined as

$$\|z\|_{TV} = \sum_{\mathbf{n} \in \Omega} \|\nabla z[\mathbf{n}]\|, \quad (2)$$

where $\|\cdot\|$ is the usual Euclidean norm and $\nabla z[\mathbf{n}]$ is the discrete gradient of z at location \mathbf{n} , calculated using finite backward differences:

$$\nabla z[\mathbf{n}] = [z[\mathbf{n}] - z[\mathbf{n} - (1, 0)], z[\mathbf{n}] - z[\mathbf{n} - (0, 1)]], \quad (3)$$

with periodic boundary conditions. TV regularization amounts to a prior of sparsity of the gradient in natural images; hence, it favors solutions which are piecewise smooth with sharp discontinuities, inducing sharp object contours in the image. It is thus desirable to introduce the total variation in the pansharpening model, so as to keep the geometrical information of the Pan image.

Palsson *et al.* [35] proposed a variational formulation for pansharpening. They make use of the traditional assumption that the Pan image can be represented as a linear combination of the bands of the high resolution fused image. The observation model is presented as

$$\mathbf{y} = \mathbf{M}\mathbf{v} + \mathbf{w}, \quad (4)$$

where

$$\mathbf{y} = \begin{pmatrix} \mathbf{u} \\ \mathbf{p} \end{pmatrix}, \quad \mathbf{M} = \begin{pmatrix} \mathbf{M}_1 \\ \mathbf{M}_2 \end{pmatrix},$$

with \mathbf{M}_1 denoting a decimation matrix for downsampling and \mathbf{w} representing additive Gaussian noise. Suppose that the MS image contains four bands; then $\mathbf{M}_2 = \{\frac{1}{4}\mathbf{I}, \frac{1}{4}\mathbf{I}, \frac{1}{4}\mathbf{I}, \frac{1}{4}\mathbf{I}\}$. Based on a direct TV regularization, the optimization problem for pansharpening is defined in [35] as

$$\underset{\mathbf{v}}{\text{minimize}} \|\mathbf{M}\mathbf{v} - \mathbf{y}\|_2^2 + \lambda \sum_{i=1}^L \|\mathbf{v}_i\|_{TV}. \quad (5)$$

As mentioned in the Introduction, the ideal assumption that the Pan band is an average of the high resolution MS image bands may lead to spectral distortion. Moreover, the sum of the total variation of the individual bands does not favor discontinuities at the same place in the different bands, contrary to what is systematically observed in real images.

Another way of regularizing the problem of estimating \mathbf{v} given \mathbf{u} and \mathbf{p} consists in solving an optimization problem of the form

$$\underset{\mathbf{v}}{\text{minimize}} (1/2)\|\mathcal{R}\mathbf{v} - \mathbf{u}\|_2^2 + \phi(\mathbf{v}, \mathbf{p}), \quad (6)$$

where the data fidelity term $(1/2)\|\mathcal{R}\mathbf{v} - \mathbf{u}\|_2^2$ measures the data misfit with respect to \mathbf{u} and the regularizer $\phi(\mathbf{v}, \mathbf{p})$ promotes a solution \mathbf{v} with desired properties, which depend on the Pan image \mathbf{p} . In this vein, the authors of [30] proposed to add the

gradient of the Pan image into the total variation functional, in order to inject important geometric and structural information of the Pan image into the fused image. The optimization problem is defined in [30] as

$$\underset{\mathbf{v}}{\text{minimize}} \|\mathcal{R}\mathbf{v} - \mathbf{u}\|_2^2 + \lambda \|\langle \mathbf{v}, \mathbf{p} \rangle\|_{ETV}, \quad (7)$$

where $\lambda > 0$ is the regularization parameter and $\|\langle \mathbf{v}, \mathbf{p} \rangle\|_{ETV}$ is an extended version of the total variation defined as

$$\|\langle \mathbf{v}, \mathbf{p} \rangle\|_{ETV} = \sum_{\mathbf{n} \in \Omega} \sqrt{\|\nabla \mathbf{v}_1[\mathbf{n}]\|^2 + \dots + \|\nabla \mathbf{v}_L[\mathbf{n}]\|^2 + a^2 \|\nabla \mathbf{p}[\mathbf{n}]\|^2}, \quad (8)$$

where the parameter a controls the importance of the geometric information of the Pan image in the fused image. A small value of a will lead to similar results as with the classical total variation, whereas a large value of a gives more emphasis to the information of the Pan image. Note that there is an important difference between the truly vectorial TV in (8) and the separable form in (5), used in [35]: only the former promotes spatially aligned discontinuities across the MS bands, as expected in natural images.

III. PROPOSED APPROACH

To go beyond the relatively simple regularization functionals presented in the previous section, we must remark that both \mathbf{p} and \mathbf{v} are integrations of the underlying continuous spectra using different channel responses. Given that the support of the spectral response of the Pan channel contains those of the MS channels, there is a strong dependency between \mathbf{v} and \mathbf{p} . To shed light on this issue, let $\mathbf{s}[\mathbf{n}] \in \mathbb{R}^B$ stand for a discrete representation of the true continuous reflectance spectra at given pixel indexed by \mathbf{n} with $B \gg L$ bands covering the Pan and MS wavelengths. We have then

$$\begin{bmatrix} \mathbf{v}[\mathbf{n}] \\ \mathbf{p}[\mathbf{n}] \end{bmatrix} = \underbrace{\begin{bmatrix} \mathbf{A}_m^T \\ \mathbf{a}_p^T \end{bmatrix}}_{\mathbf{A}^T} \mathbf{s}[\mathbf{n}], \quad (9)$$

where the columns of \mathbf{A}_m and the vector \mathbf{a}_p hold, respectively, the spectral responses of the MS channels and of the Pan channel. Expression (9) unveils two important links between images \mathbf{v} and \mathbf{p} ; one is spatial and the other spectral. Below, we address these links and explain the way they are herein exploited to build the regularizer $\phi(\mathbf{v}, \mathbf{p})$.

A. Spatial Links Between the MS and the Pan Images

From (9), it is evident that the spatial variations of \mathbf{v} and of \mathbf{p} on a given location are caused by the spatial variations of \mathbf{s} in the same locations. Therefore, it makes sense to promote solutions \mathbf{v} with high frequency content at the same locations as in the Pan image. In practice, this is achieved by using the extended total variation (ETV) seminorm defined in (8). For a given pixel \mathbf{n} , if the weight a in (8) is much larger than one, the discrete gradients $\nabla \mathbf{v}_i[\mathbf{n}]$ have little influence on the value of $\|\langle \mathbf{v}, \mathbf{p} \rangle\|_{ETV}$, whenever the value of $\|\nabla \mathbf{p}[\mathbf{n}]\|$ is large. Therefore, setting $a \gg 1$ promotes solutions \mathbf{v} where the discrete differences $\nabla \mathbf{v}_i[\mathbf{n}]$ with large amplitude are spatially aligned with those of \mathbf{p} .

B. Spectral Links Between the MS and the Pan Images

From expression (9), we obtain the projection of $\mathbf{s}[\mathbf{k}]$ on the range of \mathbf{A}_m as

$$\mathbf{s}_{\parallel}[\mathbf{n}] = (\mathbf{A}_m^T)^{\#} \mathbf{v}[\mathbf{n}],$$

where $(\mathbf{A}_m^T)^{\#}$ denotes the right inverse of \mathbf{A}_m^T , which exists because the columns of \mathbf{A}_m are linearly independent. Decomposing $\mathbf{s}[\mathbf{n}] = \mathbf{s}_{\parallel}[\mathbf{n}] + \mathbf{s}_{\perp}[\mathbf{n}]$, where $\mathbf{s}_{\perp}[\mathbf{n}]$ is the projection of $\mathbf{s}[\mathbf{n}]$ onto the null space of \mathbf{A}_m^T , and making use of the last equation of (9), we may write

$$\mathbf{p}[\mathbf{n}] = \boldsymbol{\alpha}^T \mathbf{v}[\mathbf{n}] + \boldsymbol{\epsilon}[\mathbf{n}], \quad (10)$$

where $\boldsymbol{\alpha}^T = \mathbf{a}_p^T (\mathbf{A}_m^T)^{\#}$ and $\boldsymbol{\epsilon}[\mathbf{n}] = \mathbf{a}_p^T \mathbf{s}_{\perp}[\mathbf{n}]$. Expression (10) states that the Pan band is given by a linear combination of the MS bands plus an unknown component. Since, in a given scene, the spectrum \mathbf{s} belongs very often to a low dimensional subspace of smooth functions, not far from the range of \mathbf{A}_m , the magnitude of the unknown component $\boldsymbol{\epsilon}[\mathbf{n}]$ tends to be small.

At this point, we want to remark that numerous works have exploited the linear constraint $\mathbf{p}[\mathbf{n}] = \boldsymbol{\alpha}^T \mathbf{v}[\mathbf{n}]$ (see [3], [28], [29], and references therein). However, a careless enforcement of this constraint yields often poor inferences, owing to the presence of the error $\boldsymbol{\epsilon}$ in (10) and to the use of poor approximations for the regression vector $\boldsymbol{\alpha}$. In this paper, we cope with these two drawbacks by using (10) as a soft constraint and by accurately estimating the regression vector $\boldsymbol{\alpha}$ from the data.

Assume that the linear operator \mathcal{R} acts equally on all bands by applying the same convolution operator to all bands, represented by matrix $\mathbf{C}_b \in \mathbb{R}^{N \times N}$, followed by downsampling in space. Under these circumstances, and from (10), we may write

$$\mathbf{C}_b \mathbf{p} = \sum_{l=1}^L \alpha_l \mathbf{C}_b \mathbf{v}_l + \mathbf{C}_b \boldsymbol{\epsilon}. \quad (11)$$

Expression (11) points the way to estimating $\boldsymbol{\alpha}$ from the observed Pan and low resolution MS images: since $\mathbf{u} = \mathcal{R}\mathbf{v} + \mathbf{w}$, we can find $\boldsymbol{\alpha}$ by computing a linear regression between $\mathbf{C}_b \mathbf{p}[n_1 S, n_2 S]$ and $\mathbf{u}[n_1, n_2]$ for $n_1 = 1, \dots, N_1/S$ and $n_2 = 1, \dots, N_2/S$.

C. The Proposed Pansharpening Inference Criteria

Based on the rationale developed in the above Sections (III-A) and (III-B), we introduce the following regularizer:

$$\phi_1(\mathbf{v}, \mathbf{p}) = (\lambda_\beta/2) \left\| \mathbf{p} - \boldsymbol{\beta}^T \mathbf{v} \right\|_2^2 + \lambda_{TV} \|(\mathbf{v}, \mathbf{p})\|_{ETV}, \quad (12)$$

where $\boldsymbol{\beta} = \boldsymbol{\alpha} \otimes \mathbf{1}_{S^2 N}$, \otimes denotes Kronecker multiplication, and $\mathbf{1}_m$ denotes a column vector size m containing only ones. The term $\left\| \mathbf{p} - \boldsymbol{\beta}^T \mathbf{v} \right\|_2^2$ in ϕ_1 promotes linear dependence between the Pan band and the MS bands and the term $\|(\mathbf{v}, \mathbf{p})\|_{ETV}$ promotes alignment of the high frequency components of \mathbf{v} with those of \mathbf{p} .

Because of limitations of spaceborne sensors, remote sensed image may contain outliers such as noise and missing or corrupted pixels. To cope with these degradation mechanisms,

and inspired by the work of Candès *et al.* [36], we introduce another pansharpening regularizer, which is a robust version of ϕ_1 where the quadratic term $\left\| \mathbf{p} - \boldsymbol{\beta}^T \mathbf{v} \right\|_2^2$ is replaced by a weighted combination of the nuclear norm $\|\mathbf{A}\|_* = \sum_i \sigma_i(\mathbf{A})$ ($\sigma_i(\mathbf{A})$ denotes the i th singular value of \mathbf{A}) and the ℓ_1 norm $\|\mathbf{A}\|_1 = \sum_{ij} |[A]_{ij}|$. The proposed regularizer is given by

$$\phi_2(\mathbf{v}, \mathbf{p}, \mathbf{q}) = \lambda_* \|[\text{vec}^{-1}(\mathbf{v}), \mathbf{q}]\|_* + \lambda_1 \|\mathbf{q} - \mathbf{p}\|_1 + \lambda_{TV} \|(\mathbf{v}, \mathbf{q})\|_{ETV}, \quad (13)$$

where the optimization variables are $\mathbf{v} \in \mathbb{R}^{NL}$ and $\mathbf{q} \in \mathbb{R}^N$. We remark that $\text{vec}^{-1}(\mathbf{v})$ maps vector of size NL into a matrix with N rows and L columns. So, the matrix $[\text{vec}^{-1}(\mathbf{v}), \mathbf{q}]$ has N rows and $L + 1$ columns.

In spite of a different structure, the regularizers $\phi_1(\mathbf{v}, \mathbf{p})$ and $\phi_2(\mathbf{v}, \mathbf{p}, \mathbf{q})$ are strongly related. For a while, let us assume that $\mathbf{q} = \mathbf{p}$. In this case, the last term of (13) is as in ϕ_1 and the first term promotes linear dependence among the $L + 1$ bands of (\mathbf{v}, \mathbf{p}) . We remark that the term $\left\| \mathbf{p} - \boldsymbol{\beta}^T \mathbf{v} \right\|_2^2$ in ϕ_1 also promotes linear dependence, although this dependence is only between the Pan band and the MS bands. We conclude, therefore, that in the case $\mathbf{q} = \mathbf{p}$, ϕ_1 and ϕ_2 are strongly related. For $\mathbf{q} \neq \mathbf{p}$, the presence of the ℓ_1 regularizer promotes solutions with $\mathbf{p}[\mathbf{n}] = \mathbf{q}[\mathbf{n}]$ in most pixels, apart from a set of outliers in which \mathbf{p} and \mathbf{q} become “disconnected”. Therefore, the ℓ_1 introduces robustness with respect to the linear dependence assumption.

With the recent increase in attention given to low-rank matrix recovery in compressive sensing, Candès and Plan have shown that a robust recovery can be obtained by properly constrained trace norm minimization [37]. In particular, the minimization of a weighted combination of the trace norm and of the ℓ_1 norm, called Principal Component Pursuit (PCP), may recover successfully both the low-rank and the sparse components in a data matrix [36]. Applications for PCP are widespread, such as video surveillance, face recognition, latent semantic indexing, or graphic model learning [38]. In the field of remote sensing, high spectral resolution images are demonstrated to have low-rank structure, due to correlations among the spectral bands [39], [40]. Therefore, it is natural to introduce the PCP ideas into the pansharpening process.

In conclusion, aiming at obtaining fused images that preserve both low-rank structure of the MS image and important geometric details of the Pan image, we introduce the following two pansharpening inference criteria:

$$\begin{aligned} \text{LR-TV} \quad & \underset{\mathbf{v}}{\text{minimize}} \quad (1/2) \left\| \mathcal{R}\mathbf{v} - \mathbf{u} \right\|_2^2 + (\lambda_\beta/2) \left\| \mathbf{p} - \boldsymbol{\beta}^T \mathbf{v} \right\|_2^2 \\ & + \lambda_{TV} \|(\mathbf{v}, \mathbf{p})\|_{ETV} \end{aligned} \quad (14)$$

$$\begin{aligned} \text{PCP-TV} \quad & \underset{\mathbf{v}, \mathbf{q}}{\text{minimize}} \quad (1/2) \left\| \mathcal{R}\mathbf{v} - \mathbf{u} \right\|_2^2 + \lambda_* \|[\text{vec}^{-1}(\mathbf{v}), \mathbf{q}]\|_* \\ & + \lambda_1 \|\mathbf{q} - \mathbf{p}\|_1 + \lambda_{TV} \|(\mathbf{v}, \mathbf{q})\|_{ETV}. \end{aligned} \quad (15)$$

The designations LR-TV and PCP-TV are associated to the respective regularizers, where TV stands for total variation, LR for linear regression, and PCP for principal component pursuit. The positive Lagrangian parameters λ_β and λ_{TV} in LR-TV and $\lambda_*, \lambda_1, \lambda_{TV}$ in PCP-TV control the trade-off between the antagonist criteria.

TABLE I
LR-TV LINEAR OPERATORS

1) $\mathbf{A}_p = [0, 0, \dots, 0, 1] \otimes \mathbf{I}$	$\mathbf{A}_p \mathbf{x} = \mathbf{x}_{L+1}$	Select Pan band
2) $\mathbf{C} = [\mathbf{I}_L, \mathbf{0}] \otimes \mathbf{C}_b$	$\mathbf{C}\mathbf{x} = \text{vec}([\mathbf{C}_b\mathbf{x}_1, \dots, \mathbf{C}_b\mathbf{x}_L])$	MS spatial convolution
3) $\mathbf{M} = \mathbf{I}_L \otimes \mathbf{M}_b$	$\mathbf{M}\mathbf{v} = \text{vec}([\mathbf{M}_b\mathbf{v}_1, \dots, \mathbf{M}_b\mathbf{v}_L])$	MS spatial downsampling
4) $\mathbf{A}_\alpha = \mathbf{a}^T \otimes \mathbf{I}$	$\mathbf{A}_\alpha \mathbf{x} = \sum_{i=1}^L \alpha_i \mathbf{x}_i - \mathbf{x}_{L+1}$	Spectral linear regression
5) $\mathbf{D} = \begin{bmatrix} \mathbf{D}^h \\ \mathbf{D}^v \end{bmatrix} = \begin{bmatrix} \text{diag}(\boldsymbol{\omega}) \otimes \mathbf{D}_b^h \\ \text{diag}(\boldsymbol{\omega}) \otimes \mathbf{D}_b^v \end{bmatrix}$	$\mathbf{D}\mathbf{x} = \begin{bmatrix} \text{vec}(\mathbf{D}_b^h \mathbf{X} \text{diag}(\boldsymbol{\omega})) \\ \text{vec}(\mathbf{D}_b^v \mathbf{X} \text{diag}(\boldsymbol{\omega})) \end{bmatrix}$	Discrete gradient

TABLE II
PCP-TV LINEAR OPERATORS

1) $\mathbf{A}_p = [0, 0, \dots, 0, 0, 1] \otimes \mathbf{I}$	$\mathbf{S}\mathbf{x} = \mathbf{x}_{L+2}$	Select Pan band
2) $\mathbf{C} = [\mathbf{I}_L, \mathbf{0}] \otimes \mathbf{C}_b$	$\mathbf{C}\mathbf{x} = \text{vec}([\mathbf{C}_b\mathbf{x}_1, \dots, \mathbf{C}_b\mathbf{x}_L])$	MS spatial convolution
3) $\mathbf{M} = \mathbf{I}_L \otimes \mathbf{M}_b$	$\mathbf{M}\mathbf{v} = \text{vec}([\mathbf{M}_b\mathbf{v}_1, \dots, \mathbf{M}_b\mathbf{v}_L])$	MS spatial downsampling
4) $\mathbf{V} = [\mathbf{I}_{L+1}, \mathbf{0}] \otimes \mathbf{I}$	$\mathbf{V}\mathbf{x} = \text{vec}([\mathbf{x}_1, \dots, \mathbf{x}_{L+1}])$	Select MS + q
5) $\mathbf{A}_r = [0, 0, \dots, 0, 1, -1] \otimes \mathbf{I}$	$\mathbf{A}_r \mathbf{x} = \mathbf{x}_{L+1} - \mathbf{x}_{L+2}$	Spectral linear regression
6) $\mathbf{D} = \begin{bmatrix} \mathbf{D}^h \\ \mathbf{D}^v \end{bmatrix} = \begin{bmatrix} \text{diag}(\boldsymbol{\omega}, 0) \otimes \mathbf{D}_b^h \\ \text{diag}(\boldsymbol{\omega}, 0) \otimes \mathbf{D}_b^v \end{bmatrix}$	$\mathbf{D}\mathbf{x} = \begin{bmatrix} \text{vec}(\mathbf{D}_b^h \mathbf{X} \text{diag}(\boldsymbol{\omega}, 0)) \\ \text{vec}(\mathbf{D}_b^v \mathbf{X} \text{diag}(\boldsymbol{\omega}, 0)) \end{bmatrix}$	Discrete gradient

We note that a constraint of nonnegativity for the pixel values of an image could be added in the optimization problem, but the difference between the solutions would not be significant for an increased complexity of the algorithm.

IV. OPTIMIZATION ALGORITHMS

In this Section, we develop two algorithms, inspired by the Split Augmented Lagrangian Shrinkage (SALSA) methodology introduced in [41], to solve the LR-TV and the PCP-TV optimizations. We start by rewriting the LR-TV and the PCP-TV optimization problems in a format more suitable to SALSA [41].

A. LR-TV Optimization

Let us define the matrix $\mathbf{X} = [\mathbf{x}_1, \dots, \mathbf{x}_L, \mathbf{x}_{L+1}]$ and its vectorized representation $\mathbf{x} = \text{vec}([\mathbf{x}_1, \dots, \mathbf{x}_L, \mathbf{x}_{L+1}]) = [\mathbf{v}^T, \mathbf{p}^T]^T$; that is, $\mathbf{x}_n = \mathbf{v}_n$, for $n = 1, \dots, L$, hold the L bands of the high resolution pansharpened image and \mathbf{x}_{L+1} holds the panchromatic image. In addition, the symbol \otimes stands for the Kronecker product, $\text{diag}(\boldsymbol{\omega})$, with $\boldsymbol{\omega} = [\omega_1, \dots, \omega_p]^T$, stands for a diagonal matrix with diagonal elements $\omega_1, \dots, \omega_p$, and $\mathbf{a} = [\alpha_1, \alpha_2, \dots, \alpha_L, -1]^T$. Table I lists the definitions of the matrices representing the linear operators used in the LR-TV formulation.

The matrix $\mathbf{C}_b \in \mathbb{R}^{N \times N}$ in the definition of \mathbf{C} implements a cyclic convolution modeling the sensor PSF¹. The matrix $\mathbf{M}_b \in \mathbb{R}^{N/S^2 \times N}$ in the definition of \mathbf{M} accounts for the MS spatial downsampling; the matrices $\mathbf{D}_b^h, \mathbf{D}_b^v \in \mathbb{R}^{N \times N}$ in the definition of \mathbf{D} compute horizontal and vertical first order backward differences, respectively, and the weights $\omega_1, \dots, \omega_{L+1}$ allow to weight the $L + 1$ bands in a non-uniform fashion, with relevance to the Pan band as discussed in Section III.

¹The subindex b indicates that the matrix acts on the bands.

With these definitions in place, the LR-TV optimization may be written as

$$\begin{aligned} & \underset{\mathbf{x}}{\text{minimize}} \quad (1/2) \|\mathbf{MCx} - \mathbf{u}\|_2^2 + \lambda_{TV} \phi(\mathbf{D}\mathbf{x}) \\ & \quad + (\lambda_\beta/2) \|\mathbf{A}_\alpha \mathbf{x}\|_2^2 \\ & \text{subject to } \mathbf{A}_p \mathbf{x} = \mathbf{p}, \end{aligned} \quad (16)$$

where

$$\phi(\mathbf{D}\mathbf{x}) = \sum_{\mathbf{n} \in \Omega} \sqrt{\|\mathbf{D}^h \mathbf{x}[\mathbf{n}]\|_2^2 + \|\mathbf{D}^v \mathbf{x}[\mathbf{n}]\|_2^2} \quad (17)$$

is an alternative way of expressing the ETV regularizer $\|(\mathbf{v}, \mathbf{p})\|_{ETV}$ introduced in (8).

B. PCP-TV Optimization

In a way similar to the definitions introduced in Section IV-A, let us define $\mathbf{X} = [\mathbf{x}_1, \dots, \mathbf{x}_L, \mathbf{x}_{L+1}, \mathbf{x}_{L+2}]$ and its vectorized representation $\mathbf{x} = \text{vec}([\mathbf{x}_1, \dots, \mathbf{x}_L, \mathbf{x}_{L+1}, \mathbf{x}_{L+2}]) = [\mathbf{v}^T, \mathbf{q}^T, \mathbf{p}^T]^T$. The linear operators used in the PCP-TV formulation are presented in Table II.

With these definitions in place, the PCP-TV optimization may be written as

$$\begin{aligned} & \underset{\mathbf{x}}{\text{minimize}} \quad (1/2) \|\mathbf{MCx} - \mathbf{u}\|_2^2 + \lambda_{TV} \phi(\mathbf{D}\mathbf{x}) \\ & \quad + \lambda_* \left\| \text{vec}^{-1}(\mathbf{V}\mathbf{x}) \right\|_* + \lambda_1 \|\mathbf{A}_r \mathbf{x}\|_1 \\ & \text{subject to } \mathbf{A}_p \mathbf{x} = \mathbf{p}. \end{aligned} \quad (18)$$

C. Unified Formulation for LR-TV and PCP-TV Optimization

Both optimization problems (16) and (18) may be written as

$$\underset{\mathbf{x}}{\text{minimize}} \quad \sum_{i=1}^J g_i(\mathbf{H}_i \mathbf{x}) \quad \text{subject to } \mathbf{H}_0 \mathbf{x} = \mathbf{p}, \quad (19)$$

where g_i , for $i = 1, \dots, J$, denote closed, proper, and convex functions, and \mathbf{H}_i , for $i = 0, 1, \dots, J$, denote linear operators.

TABLE III

DEFINITIONS OF THE ENTITIES USED IN UNIFIED FORMULATION FOR LR-TV AND PCP-TV OPTIMIZATION (OPTIMIZATION PROBLEM (19))

LR-TV($J = 3$) $\mathbf{H}_0 = \mathbf{A}_p, \mathbf{H}_1 = \mathbf{C}, \mathbf{H}_2 = \mathbf{D}, \mathbf{H}_3 = \mathbf{I}$ $g_1(\boldsymbol{\xi}) = (1/2) \ \mathbf{M}\boldsymbol{\xi} - \mathbf{u}\ _2^2$ $g_2(\boldsymbol{\xi}) = \lambda_{TV} \sum_{\mathbf{n} \in \Omega} \sqrt{\ \boldsymbol{\xi}^h[\mathbf{n}]\ _2^2 + \ \boldsymbol{\xi}^v[\mathbf{n}]\ _2^2}$ $g_3(\boldsymbol{\xi}) = (\lambda_\beta/2) \ \mathbf{A}_\alpha \boldsymbol{\xi}\ _2^2$	PCP-TV($J = 4$) $\mathbf{H}_0 = \mathbf{A}_p, \mathbf{H}_1 = \mathbf{C}, \mathbf{H}_2 = \mathbf{D}, \mathbf{H}_3 = \mathbf{V},$ $\mathbf{H}_4 = \mathbf{I}$ $g_1(\boldsymbol{\xi}) = (1/2) \ \mathbf{M}\boldsymbol{\xi} - \mathbf{u}\ _2^2$ $g_2(\boldsymbol{\xi}) = \lambda_{TV} \sum_{\mathbf{n} \in \Omega} \sqrt{\ \boldsymbol{\xi}^h[\mathbf{n}]\ _2^2 + \ \boldsymbol{\xi}^v[\mathbf{n}]\ _2^2}$ $g_3(\boldsymbol{\xi}) = \lambda_* \ \text{vec}^{-1}(\boldsymbol{\xi})\ _*$ $g_4(\boldsymbol{\xi}) = \lambda_1 \ \mathbf{A}_r \boldsymbol{\xi}\ _1$
---	--

The specific definitions of these entities are given in Table III, where $\boldsymbol{\xi}$ are dummy variables whose dimensions depend on the functions g_i , for $i = 1, 2, 3, 4$. In the case of g_2 , we have $\boldsymbol{\xi} = [(\boldsymbol{\xi}^h)^T, (\boldsymbol{\xi}^v)^T]^T$ where $\boldsymbol{\xi}^h$ and $\boldsymbol{\xi}^v$ are in the range of \mathbf{D}^h and \mathbf{D}^v , respectively.

We now introduce the variable splitting $\mathbf{z}_i = \mathbf{H}_i \mathbf{x}$, for $i = 1, \dots, J$, in (19) and convert the original optimization into the equivalent constrained form

$$\underset{\mathbf{z}, \mathbf{x}}{\text{minimize}} \sum_{i=1}^J g_i(\mathbf{z}_i) \quad \text{subject to} \quad \mathbf{Fz} = \mathbf{Gx} + \mathbf{b}, \quad (20)$$

where $\mathbf{z}_i \in \mathbb{R}^{n_{z_i}}$, $\mathbf{z} = [\mathbf{z}_1^T, \dots, \mathbf{z}_J^T]^T \in \mathbb{R}^{n_z}$ with $n_z = n_{z_1} + n_{z_2} + \dots + n_{z_J}$, and

$$\begin{aligned} \mathbf{F} &= \left[\mathbf{0}_{N \times n_z}^T \quad \mathbf{I}_{n_z} \right]^T \\ \mathbf{G} &= [\mathbf{H}_0^T, \mathbf{H}_1^T, \mathbf{H}_2^T, \dots, \mathbf{H}_J^T]^T \\ \mathbf{b} &= [-\mathbf{p}^T, \mathbf{0}_{n_{z_1}}^T, \dots, \mathbf{0}_{n_{z_J}}^T]^T. \end{aligned}$$

The next step consists in applying a minor modification of SALSA methodology [41] to (20). SALSA is essentially an instance of the alternating method of multipliers (ADMM) [42]–[44] designed to optimize sums of an arbitrary number of convex terms. The following is a simplified version of a theorem by Eckstein and Bertsekas, adapted to our setting, stating convergence of SALSA [42]–[44]. The notation $\mathbf{d} = [\mathbf{d}_0^T, \mathbf{d}_1^T \dots \mathbf{d}_J^T]^T$ stands for scaled Lagrange multipliers associated with the equality constraint $\mathbf{Fz} = \mathbf{Gx} + \mathbf{b}$, where $\dim(\mathbf{d}_i) = \dim(\mathbf{H}_i \mathbf{x})$.

Theorem 1: Assume that \mathbf{G} is full column rank and let $f(\mathbf{z}) = \sum_{i=1}^J g_i(\mathbf{z}_i)$ be closed, proper, and convex. Consider arbitrary $\mu > 0$ and $\mathbf{z}_0, \mathbf{d}_0$. Consider three sequences $\{\mathbf{x}^k, k = 0, 1, \dots\}$, $\{\mathbf{z}^k, k = 0, 1, \dots\}$, and $\{\mathbf{d}^k, k = 0, 1, \dots\}$ that satisfy

$$\mathbf{x}^{k+1} = \arg \min_{\mathbf{x}} \|\mathbf{Gx} - \mathbf{Fz}^k + \mathbf{b} - \mathbf{d}^k\|_2^2 \quad (21)$$

$$\mathbf{z}^{k+1} = \arg \min_{\mathbf{z}} f(\mathbf{z}) + \frac{\mu}{2} \|\mathbf{Gx}^{k+1} - \mathbf{Fz} + \mathbf{b} - \mathbf{d}\|_2^2 \quad (22)$$

$$\mathbf{d}^{k+1} = \mathbf{d}^k - [\mathbf{Gx}^{k+1} - \mathbf{Fz}^{k+1} + \mathbf{d}]. \quad (23)$$

Then, if (20) has a solution, the sequence $\{\mathbf{x}^k\}$ converges to it; otherwise, at least one of the sequences $\{\mathbf{z}^k\}$ or $\{\mathbf{d}^k\}$ diverges.

Given that the matrix \mathbf{G} in both optimization problems (16) and (18) has full rank and that the objective functions are closed, proper, and convex and coercive², thus having

²Although we do not prove it, we claim that the objective functions in (16) and (18) are coercive, i.e. their value tends to $+\infty$ when $\|\mathbf{x}\| \rightarrow +\infty$, if the constant images are not in the null space of the linear operator \mathcal{R} and $\omega_i > 0$ for $i = 1, \dots, L + 1$.

Algorithm PanSALSA

```

1. Set  $k = 0$ , choose  $\mu > 0$ ,  $\mathbf{z}^0 = (\mathbf{z}_1^0, \mathbf{z}_2^0, \dots, \mathbf{z}_J^0)$ 
2. Set  $\mathbf{d}^0 = (\mathbf{d}_1^0, \mathbf{d}_2^0, \dots, \mathbf{d}_J^0, \mathbf{d}_{J+1}^0)$ 
3. repeat
4.   (* update  $\mathbf{x}$  *)
5.    $\mathbf{x}^{k+1} := \arg \min_{\mathbf{x}} \|\mathbf{Gx} - \mathbf{Fz}^k + \mathbf{b} - \mathbf{d}^k\|_2^2$ 
6.   (* update  $\mathbf{z}$  *)
7.    $\boldsymbol{\nu}_1 := \mathbf{H}_1 \mathbf{x}^{k+1} - \mathbf{d}_1^k$ 
8.    $\mathbf{z}_1^{k+1} := \arg \min_{\mathbf{z}_1} g_1(\mathbf{z}_1) + \frac{\mu}{2} \|\mathbf{z}_1 - \boldsymbol{\nu}_1\|_2^2$ 
9.    $\boldsymbol{\nu}_2 := \mathbf{H}_2 \mathbf{x}^{k+1} - \mathbf{d}_2^k$ 
10.   $\mathbf{z}_2^{k+1} := \arg \min_{\mathbf{z}_2} g_2(\mathbf{z}_2) + \frac{\mu}{2} \|\mathbf{z}_2 - \boldsymbol{\nu}_2\|_2^2$ 
11.  :
12.   $\boldsymbol{\nu}_J := \mathbf{H}_J \mathbf{x}^{k+1} - \mathbf{d}_J^k$ 
13.   $\mathbf{z}_J^{k+1} := \arg \min_{\mathbf{z}_J} g_J(\mathbf{z}_J) + \frac{\mu}{2} \|\mathbf{z}_J - \boldsymbol{\nu}_J\|_2^2$ 
14.  (* update Lagrange multipliers  $\mathbf{d}$  *)
15.   $\mathbf{d}_1^{k+1} := -\boldsymbol{\nu}_1 + \mathbf{z}_1^{k+1}$ 
16.   $\mathbf{d}_2^{k+1} := -\boldsymbol{\nu}_2 + \mathbf{z}_2^{k+1}$ 
17.  :
18.   $\mathbf{d}_3^{k+1} := -\boldsymbol{\nu}_J + \mathbf{z}_3^{k+1}$ 
19.   $k \leftarrow k + 1$ 
20. until stopping criterion is satisfied.

```

Fig. 1. Pansharpening via Augmented Lagrangian Shrinkage Algorithm (PanSALSA).

solutions, then the sequence \mathbf{x}^k generated by (21)-(22)-(23) converges to a solution of (20) for any $\mu > 0$.

Fig. 1 shows the pseudocode of the derived algorithm, which we term Pansharpening via Augmented Lagrangian Shrinkage Algorithm (PanSALSA). A distinctive feature of PanSALSA, and of any SALSA instance, is that optimization with respect to \mathbf{z} is decoupled into optimization problems with respect to the blocks \mathbf{z}_i , for $i = 1, \dots, J$, whose solutions are the so-called Moreau proximity operators [45] for the respective convex functions g_i , for $i = 1, \dots, J$. In order to implement SALSA, we need to solve the quadratic optimization problem in line 5 and to apply the Moreau proximity operators in lines 5, 8, 10, ..., 13. Below, we present the solutions to these optimization subproblems.

D. Optimization With Respect to \mathbf{x}

The solution of the quadratic optimization (21) is given by

$$\begin{aligned} \mathbf{x}^{k+1} &= (\mathbf{G}^T \mathbf{G})^{-1} \mathbf{G}^T (\mathbf{Fz}^k - \mathbf{b} + \mathbf{d}^k) \\ &= \left(\sum_{i=0}^J \mathbf{H}_i^T \mathbf{H}_i \right)^{-1} \left(\mathbf{H}_0^T (\mathbf{p} + \mathbf{d}_0^k) + \sum_{i=1}^J \mathbf{H}_i^T (\mathbf{z}_i^k + \mathbf{d}_i^k) \right) \end{aligned}$$

TABLE IV
DETAILS FOR THE COMPUTATION OF $\mathbf{H}_i^T \mathbf{H}_i$ INVOLVED IN THE OPTIMIZATION WITH RESPECT TO \mathbf{x}

LR-TV	PCP-TV
$\mathbf{H}_0^T \mathbf{H}_0 = \text{diag}([0, \dots, 0, 1]) \otimes \mathbf{I}$	$\mathbf{H}_0^T \mathbf{H}_0 = \text{diag}([0, \dots, 0, 1]) \otimes \mathbf{I}$
$\mathbf{H}_1^T \mathbf{H}_1 = \text{diag}([1, \dots, 1, 0]) \otimes \mathbf{C}_b^T \mathbf{C}_b$	$\mathbf{H}_1^T \mathbf{H}_1 = \text{diag}([1, \dots, 1, 0, 0]) \otimes \mathbf{C}_b^T \mathbf{C}_b$
$\mathbf{H}_2^T \mathbf{H}_2 = \text{diag}^2(\omega) \otimes [(\mathbf{D}_b^h)^T \mathbf{D}_b^h + (\mathbf{D}_b^v)^T \mathbf{D}_b^v]$	$\mathbf{H}_2^T \mathbf{H}_2 = \text{diag}^2(\omega, 0) \otimes [(\mathbf{D}_b^h)^T \mathbf{D}_b^h + (\mathbf{D}_b^v)^T \mathbf{D}_b^v]$
$\mathbf{H}_3^T \mathbf{H}_3 = \mathbf{I} \otimes \mathbf{I}$	$\mathbf{H}_3^T \mathbf{H}_3 = \text{diag}([1, \dots, 1, 0]) \otimes \mathbf{I}$
	$\mathbf{H}_4^T \mathbf{H}_4 = \mathbf{I} \otimes \mathbf{I}$

Having in mind the definition of \mathbf{H}_i given in Sections IV-A, IV-B, and IV-C, the computations $\mathbf{H}_i^T \xi$, for a given ξ with suitable dimensions, have computational complexity no larger than $O(LN)$, for $i \neq 2$ and $O((2NL) \ln(NL))$ for $i = 2$.

Concerning the action of $(\mathbf{G}^T \mathbf{G})^{-1}$, we note that $(\mathbf{G}^T \mathbf{G}) = \sum_{i=0}^J \mathbf{H}_i^T \mathbf{H}_i$ and that $\sum_{i=0}^J \mathbf{H}_i^T \mathbf{H}_i = \sum_{i=0}^{J+1} \Lambda_i \otimes \mathbf{T}_i$, where, for $i = 1, \dots, J+1$, Λ_i and \mathbf{T}_i are diagonal and block circulant matrices with circulant blocks, respectively. More details for the computation of $\mathbf{H}_i^T \mathbf{H}_i$ are given in Table IV.

Using the eigendecomposition of a 2D circulant matrix $\mathbf{T}_i = \mathbf{F}^H \Sigma_i \mathbf{F}$, where \mathbf{F}^H is the matrix of eigenvectors (i.e., the 2D Fourier matrix) and Σ is a diagonal matrix holding the eigenvalues of \mathbf{T}_i , we may write

$$\begin{aligned} (\mathbf{G}^T \mathbf{G}) &= \sum_{i=0}^{J+1} \Lambda_i \otimes \mathbf{T}_i = \sum_{i=0}^{J+1} \Lambda_i \otimes (\mathbf{F}^H \Sigma_i \mathbf{F}) \\ &= (\mathbf{I} \otimes \mathbf{F}^H) \left(\sum_{i=0}^{J+1} \Lambda_i \otimes \Sigma_i \right) (\mathbf{I} \otimes \mathbf{F}), \end{aligned}$$

and thus

$$(\mathbf{G}^T \mathbf{G})^{-1} = (\mathbf{I} \otimes \mathbf{F}^H) \left(\sum_{i=0}^{J+1} \Lambda_i \otimes \Sigma_i \right)^{-1} (\mathbf{I} \otimes \mathbf{F}).$$

The action of $(\mathbf{G}^T \mathbf{G})^{-1}$ on a given vector ξ is implemented as follows: compute the discrete Fourier transform (DFT) of the bands of ξ , divide elementwise by the diagonal elements of $\left(\sum_{i=1}^{J+1} \Lambda_i \otimes \Sigma_i \right)$, which are positive owing to the term $\mathbf{I} \otimes \mathbf{I}$, and finally compute the inverse discrete Fourier transform (IDFT) of each band. Using the fast Fourier transform to compute the DFTs and the IDFTs, the total complexity in computing $(\mathbf{G}^T \mathbf{G})^{-1} \xi$ is $O((L+1)N \ln N)$ in the case of LR-TV and $O((L+2)N \ln N)$ in the case of PCP-TV.

E. Moreau Proximity Operators

The optimization subproblems shown in lines 8, 10, ..., 12 correspond to evaluating the Moreau proximity operators [45] of the convex functions g_1, g_2, \dots, g_J , respectively. In this section, we present closed form expressions for these operators.

1) *Moreau Proximity Operator for g_1 (LR-TV and PCP-TV):*

$$\psi_{g_1/\mu}(\mathbf{v}) = \arg \min_{\xi} (1/2) \|\mathbf{M}\xi - \mathbf{u}\|_2^2 + (\mu/2) \|\xi - \mathbf{v}\|_2^2 \quad (24)$$

$$= (\mathbf{M}^T \mathbf{M} + \mu \mathbf{I})^{-1} (\mathbf{M}^T \mathbf{u} + \mu \mathbf{v}). \quad (25)$$

Because \mathbf{M} is a sampling matrix, $\mathbf{M}^T \mathbf{M}$ is diagonal with ones corresponding to the sampled pixels and zero elsewhere; by the same token, $\mathbf{M}^T \xi$ yields zeros for non-sampled components of ξ and leaves the sampled elements of ξ unchanged. Therefore,

$$\psi_{g_1/\mu}(\mathbf{v})[\mathbf{n}] = \begin{cases} (\mathbf{u} + \mu \mathbf{v})[\mathbf{n}] / (1 + \mu) & \text{if pixel } \mathbf{n} \text{ is sampled,} \\ \mathbf{v}[\mathbf{n}] & \text{if pixel } \mathbf{n} \text{ is not sampled.} \end{cases} \quad (26)$$

The complexity to compute $\psi_{g_1/\mu}$ is $O(NL)$.

2) *Moreau Proximity Operator for g_2 (LR-TV and PCP-TV):* The optimization problem

$$\begin{aligned} \psi_{g_2 \lambda_{TV}/\mu}(\mathbf{v}) &= \arg \min_{\xi} \lambda_{TV} \sum_{\mathbf{n} \in \Omega} \sqrt{\|\xi^h[\mathbf{n}]\|_2^2 + \|\xi^v[\mathbf{n}]\|_2^2} \\ &\quad + (\mu/2) \|\xi - \mathbf{v}\|_2^2 \end{aligned} \quad (27)$$

is pixelwise decoupled and yields the vector-soft-thresholding operator [45]

$$\psi_{g_2 \lambda_{TV}/\mu}(\mathbf{v})[\mathbf{n}] = \max \left\{ \mathbf{0}, \|\mathbf{v}[\mathbf{n}]\| - \lambda_{TV}/\mu \right\} \frac{\mathbf{v}[\mathbf{n}]}{\|\mathbf{v}[\mathbf{n}]\|}. \quad (28)$$

The complexity to compute $\psi_{g_2 \lambda_{TV}/\mu}$ is $O(N(L+1))$.

3) *Moreau Proximity Operator for g_3 (LR-TV):*

$$\begin{aligned} \psi_{g_3 \lambda_\beta/\mu}(\mathbf{v}) &= \arg \min_{\xi} (\lambda_\beta/2) \|\mathbf{A}_\alpha \xi\|_2^2 + (\mu/2) \|\xi - \mathbf{v}\|_2^2 \\ &\quad (29) \end{aligned}$$

$$= (\mathbf{A}_\alpha^T \mathbf{A}_\alpha + (\mu/\lambda_\beta) \mathbf{I})^{-1} (\mu/\lambda_\beta) \mathbf{v}. \quad (30)$$

From the definition of $\mathbf{A}_\alpha = \mathbf{a}^T \otimes \mathbf{I}$, we have

$$(\mathbf{A}_\alpha^T \mathbf{A}_\alpha + (\mu/\lambda_\beta) \mathbf{I})^{-1} = (\mathbf{a} \mathbf{a}^T + (\mu/\lambda_\beta) \mathbf{I})^{-1} \otimes \mathbf{I},$$

implying that the $\psi_{g_3 \lambda_\beta/\mu}$ acts only the spectral domain. More precisely,

$$\psi_{g_3 \lambda_\beta/\mu}(\mathbf{v})[\mathbf{n}] = (\mathbf{a} \mathbf{a}^T + (\mu/\lambda_\beta) \mathbf{I})^{-1} \mathbf{v}[\mathbf{n}].$$

The complexity to compute $\psi_{g_3 \lambda_\beta/\mu}$, in LR-TV, is $O(N(L+1)^2)$.

4) Moreau Proximity Operator for g_3 (PCP-TV):

$$\psi_{g_3\lambda_*/\mu}(\mathbf{v}) = \arg \min_{\xi} \lambda_* \|\text{vec}^{-1}(\xi)\|_* + (\mu/2) \|\xi - \mathbf{v}\|_2^2 \quad (31)$$

$$= \text{vec} \left(\mathbf{U}(\mathbf{\Lambda} - (\lambda_*/\mu)\mathbf{I})_+ \mathbf{V}^T \right), \quad (32)$$

where $\mathbf{U}\mathbf{\Lambda}\mathbf{V}^T$ is the singular value decomposition of matrix $\text{vec}^{-1}(\xi)$ and $(\cdot)_+$ denotes the nonnegative part [46].

The complexity to compute $\psi_{g_3\lambda/\mu}$, in PCP-TV, is $O(KN^2(L+1))$, with $4 \leq K \leq 22$.

5) Moreau Proximity Operator for g_4 (PCP-TV): Having in mind that $\text{vec}^{-1}(\xi) = [\xi_1 \dots, \xi_{L+2}]$ and that $\text{vec}^{-1}(\mathbf{v}) = [\mathbf{v}_1 \dots, \mathbf{v}_{L+2}]$, it follows that

$$\begin{aligned} \psi_{g_4\lambda_1/\mu}(\mathbf{v}) &= \arg \min_{\xi} \lambda_1 \|\mathbf{A}_r \xi\|_1 + (\mu/2) \|\xi - \mathbf{v}\|_2^2 \quad (33) \\ &= \arg \min_{\xi} \lambda_1 \|\xi_{L+2} - \xi_{L+1}\|_1 \\ &\quad + (\mu/2) \sum_{l=1}^{L+2} \|\xi_l - \mathbf{v}_l\|_2^2, \end{aligned} \quad (34)$$

and then [45]

$$\begin{aligned} (\psi_{g_4\lambda_1/\mu}(\mathbf{v}))_l &= \begin{cases} \mathbf{v}_l, & l = 1, \dots, L \\ (1/2)(\mathbf{v}_{L+1} + \mathbf{v}_{L+2} \\ & + \text{soft}(\mathbf{v}_{L+1} - \mathbf{v}_{L+2}, 2\lambda_1/\mu)) & l = L+1 \\ (1/2)(\mathbf{v}_{L+1} + \mathbf{v}_{L+2} \\ & - \text{soft}(\mathbf{v}_{L+1} - \mathbf{v}_{L+2}, 2\lambda_1/\mu)) & l = L+2 \end{cases} \end{aligned} \quad (35)$$

where $\text{soft}(x, \tau) = \max\{0, |x| - \tau\} \text{sign}(x)$.

The complexity to compute $\psi_{g_4\lambda_1/\mu}$, in PCP-TV, is $O(N(L+2))$.

F. PanSALSA-LR and PanSALSA-PCP Algorithms

The instances of the PanSALSA algorithm to solve the LR-TV and the PCP-TV problems (14) and (15) are shown in Figs. 2 and 3, respectively. Vector λ (line 4 of both algorithms) holds the diagonal elements $\sum_{i=0}^{J+1} \lambda_i \otimes \Sigma_i$. Recall that this matrix is diagonal and therefore completely defined by λ . The vector \mathbf{x}^{k+1} in line 8 is obtained by applying FFT to the bands of \mathbf{x} , followed by elementwise division by λ , denoted by \oslash , followed by IFFT. Lines 10-15 in PanSALSA-LR and 10-17 in PanSALSA-PCP compute the respective Moreau proximity operators, and lines 17-19 in PanSALSA-LR and 19-22 in PanSALSA-PCP update the Lagrange multipliers.

Both PanSALSA algorithms converge for any $\mu > 0$. However, the convergence speed is highly sensitive to the value of μ . This issue is currently a hot research topic. In this work, we have implemented the selection rule discussed in [47, Ch. 3.4] and therein formalized in expression (3.13). Nevertheless, we have observed experimentally that a value of $\mu \simeq 0.05$ yields nearly optimum convergence speed, provided that the MS and Pan images are scaled to the interval $[0, 1]$. Regarding the stopping criterion, we impose that the primal and dual residuals be smaller than a given threshold, as suggested in [47, Ch. 3.3.2]. Nevertheless, we have observed that a fixed

Algorithm PanSALSA-LR

```

1. Set  $k = 0$ , choose  $\mu > 0$ ,  $\lambda_{TV}$ ,  $\lambda_\beta$ 
2. Set  $\mathbf{z}^0 = (\mathbf{z}_1^0, \mathbf{z}_2^0, \mathbf{z}_3^0)$ ,  $\mathbf{d}^0 = (\mathbf{d}_1^0, \mathbf{d}_2^0, \mathbf{d}_3^0)$ 
3. Set  $\mathbf{H}_0 = \mathbf{A}_p$ ,  $\mathbf{H}_1 = \mathbf{C}$ ,  $\mathbf{H}_2 = \mathbf{D}$ ,  $\mathbf{H}_3 = \mathbf{I}$ 
4. Set  $\lambda = \text{diagonal of matrix } (\sum_{i=0}^4 \lambda_i \otimes \Sigma_i)$ 
5. repeat
   6.   (* update  $\mathbf{x}$  *)
   7.    $\xi = (\mathbf{H}_0^T(\mathbf{p} + \mathbf{d}_0^k) + \sum_{i=1}^3 \mathbf{H}_i^T(\mathbf{z}_i^k + \mathbf{d}_i^k))$ 
   8.    $\mathbf{x}^{k+1} := (\mathbf{I} \otimes \mathbf{F}^H) \{ ((\mathbf{I} \otimes \mathbf{F})\xi) \oslash \lambda \}$ 
   9.   (* update  $\mathbf{z}$  *)
  10.    $\nu_1 := \mathbf{H}_1 \mathbf{x}^{k+1} - \mathbf{d}_1^k$ 
  11.    $\mathbf{z}_1^{k+1} := \psi_{g_1\lambda/\mu}(\nu_1)$ 
  12.    $\nu_2 := \mathbf{H}_2 \mathbf{x}^{k+1} - \mathbf{d}_2^k$ 
  13.    $\mathbf{z}_2^{k+1} := \psi_{g_2\lambda_{TV}/\mu}(\nu_2)$ 
  14.    $\nu_3 := \mathbf{H}_3 \mathbf{x}^{k+1} - \mathbf{d}_3^k$ 
  15.    $\mathbf{z}_3^{k+1} := \psi_{g_3\lambda_\beta/\mu}(\nu_3)$ 
  16.   (* update Lagrange multipliers  $\mathbf{d}$  *)
  17.    $\mathbf{d}_1^{k+1} := -\nu_1 + \mathbf{z}_1^{k+1}$ 
  18.    $\mathbf{d}_2^{k+1} := -\nu_2 + \mathbf{z}_2^{k+1}$ 
  19.    $\mathbf{d}_3^{k+1} := -\nu_3 + \mathbf{z}_3^{k+1}$ 
  20.    $k \leftarrow k + 1$ 
21. until stopping criterion is satisfied.

```

Fig. 2. LR-TV algorithm.

Algorithm PanSALSA-PCP

```

1. Set  $k = 0$ , choose  $\mu > 0$ ,  $\lambda_{TV}$ ,  $\lambda_*$ ,  $\lambda_1$ 
2. Set  $\mathbf{z}^0 = (\mathbf{z}_1^0, \mathbf{z}_2^0, \mathbf{z}_3^0, \mathbf{z}_4^0)$ ,  $\mathbf{d}^0 = (\mathbf{d}_1^0, \mathbf{d}_2^0, \mathbf{d}_3^0, \mathbf{d}_4^0)$ 
3. Set  $\mathbf{H}_0 = \mathbf{A}_p$ ,  $\mathbf{H}_1 = \mathbf{C}$ ,  $\mathbf{H}_2 = \mathbf{D}$ ,  $\mathbf{H}_3 = \mathbf{V}$ ,  $\mathbf{H}_4 = \mathbf{I}$ 
4. Set  $\lambda = \text{diagonal of matrix } (\sum_{i=0}^5 \Lambda_i \otimes \Sigma_i)$ 
5. repeat
   6.   (* update  $\mathbf{x}$  *)
   7.    $\xi = (\mathbf{H}_0^T(\mathbf{p} + \mathbf{d}_0^k) + \sum_{i=1}^5 \mathbf{H}_i^T(\mathbf{z}_i^k + \mathbf{d}_i^k))$ 
   8.    $\mathbf{x}^{k+1} := (\mathbf{I} \otimes \mathbf{F}^H) \{ ((\mathbf{I} \otimes \mathbf{F})\xi) \oslash \lambda \}$ 
   9.   (* update  $\mathbf{z}$  *)
  10.    $\nu_1 := \mathbf{H}_1 \mathbf{x}^{k+1} - \mathbf{d}_1^k$ 
  11.    $\mathbf{z}_1^{k+1} := \psi_{g_1\lambda/\mu}(\nu_1)$ 
  12.    $\nu_2 := \mathbf{H}_2 \mathbf{x}^{k+1} - \mathbf{d}_2^k$ 
  13.    $\mathbf{z}_2^{k+1} := \psi_{g_2\lambda_{TV}/\mu}(\nu_2)$ 
  14.    $\nu_3 := \mathbf{H}_3 \mathbf{x}^{k+1} - \mathbf{d}_3^k$ 
  15.    $\mathbf{z}_3^{k+1} := \psi_{g_3\lambda_*/\mu}(\nu_3)$ 
  16.    $\nu_4 := \mathbf{H}_4 \mathbf{x}^{k+1} - \mathbf{d}_4^k$ 
  17.    $\mathbf{z}_4^{k+1} := \psi_{g_4\lambda_1/\mu}(\nu_4)$ 
  18.   (* update Lagrange multipliers  $\mathbf{d}$  *)
  19.    $\mathbf{d}_1^{k+1} := -\nu_1 + \mathbf{z}_1^{k+1}$ 
  20.    $\mathbf{d}_2^{k+1} := -\nu_2 + \mathbf{z}_2^{k+1}$ 
  21.    $\mathbf{d}_3^{k+1} := -\nu_3 + \mathbf{z}_3^{k+1}$ 
  22.    $\mathbf{d}_4^{k+1} := -\nu_4 + \mathbf{z}_4^{k+1}$ 
  23.    $k \leftarrow k + 1$ 
24. until stopping criterion is satisfied.

```

Fig. 3. PCP-TV algorithm.

number of iterations of the order of 200 provides excellent results.

Finally, we give an indication of the computational complexity of PanSALSA-LR and PanSALSA-PCP. Having in mind the computational complexities involved in the computation of \mathbf{x} and of the Moreau proximity operators, we conclude that the PanSALSA-LR computational complexity per iteration is dominated by the term $O((L+1)N \ln N)$, associated to the computation of \mathbf{x} , and that of PanSALSA-PCP is dominated by the term $O(K(L+1)N^2)$, associated to the SVD decomposition in the computation of the Moreau proximity operator for the nuclear norm.

TABLE V
DATA SET DESCRIPTION: PATTERN DATA

Type	simulated: $(\mathbf{v}, \mathbf{p}) = \mathbf{A}^T \mathbf{s}$, $\mathbf{s} = \mathbf{M} \mathbf{X}$
Size	$\mathbf{u}: 125 \times 125 \times 4$, $\mathbf{p}: 500 \times 500$
\mathbf{A}	IKONOS spectral responses
$\mathbf{M} \in \mathbb{R}^{224 \times 42}$	mixing matrix sampled from the USGS library
$\mathbf{X} \in \mathbb{R}^{42 \times 500^2}$	abundance matrix (only pure pixels)
\mathcal{R}	downsampling $S = 4$, PSF Gaussian (std. dev. $s_h = s_v = 1.93$)

V. EXPERIMENTAL RESULTS

In this section, we present some experimental results on several simulated and real datasets: the Pattern image simulated with the USGS library, the ROSIS Pavia image and the Pléiades satellite image. The two proposed pansharpening methods LR-TV and PCP-TV, are compared with seven state-of-the-art methods, including two recent component substitution methods with spectral adjustment: FIHS-SA³ [18] and GSA⁴ [20]; two multiresolution-analysis methods, which are joint winners of the 2006 IEEE Data Fusion Contest⁵ [13]: AWLP [23] and GLP-CBD [22], [49]; and three variational methods⁶: P+XS [28] and the two TV based methods presented in Sect. II (respectively referred to as TV_1 for the method in [30] and TV_2 for the method in [35]).

A. Parameter Setting

We solve the optimization problems (14) and (15) by the PanSALSA algorithm presented in Sect. IV, with initializations $\mathbf{v}_i = \mathbf{p}$ and $\mathbf{q} = \mathbf{p}$. The choice of the regularization parameters for each term in (14) and (15) is an important issue. For the problem of LR-TV, the two parameters λ_β and λ_{TV} need to be set, whereas for PCP-TV, we have the three parameters λ_* , λ_1 and λ_{TV} to fix. A result from the theory underlying the PCP is the optimal choice $\lambda_1 = \lambda_* / \sqrt{\max(n_1, n_2)}$, where (n_1, n_2) is the size of the matrix to be decomposed [36]. Following this recipe, we first set $\lambda_1 = \lambda_* / \sqrt{\max(N_1 N_2, L + 1)}$. It remains then to tune only two parameters λ_{TV} and λ_* . We have conducted experiments by trying different combinations of some preset values on a subset of each dataset. The optimum values are those providing the best compromise between two widely used quality indices for pansharpening: SAM and ERGAS (described in detail in the following subsection). The parameters are almost constant for all datasets. In our experiments, we set $\lambda_\beta = 10^{-2}$ and $\lambda_{TV} = 10^{-3}$ for LR-TV and $\lambda_* = 10^{-2}$, $\lambda_{TV} = 10^{-3}$ and $\lambda_1 = 10^0$ for PCP-TV. In all cases, $a = 10$. Due to space limit, we omit the details of the parameter selection and the algorithm performance here. Interested readers could refer to the Supplementary Material, which can be downloaded online⁷.

³Implemented by us. For the Pattern image and the ROSIS Pavia image, the spectral weights are the same as those obtained in the original paper, that is, the weights for the four multispectral bands (B, G, R, Nir) are (0.25, 0.75, 1, 1). For the Pléiades satellite image, the real weights are used, that is (0, 0.5, 0.5, 0).

⁴Implemented by us, with the GS spectral sharpening of ENVI.

⁵Code kindly provided by Dr. G. Vivone, which will be released soon [48].

⁶Implemented by us.

⁷<http://www.gipsa-lab.fr/jocelyn.chanussot/SupplementaryMaterial.pdf>

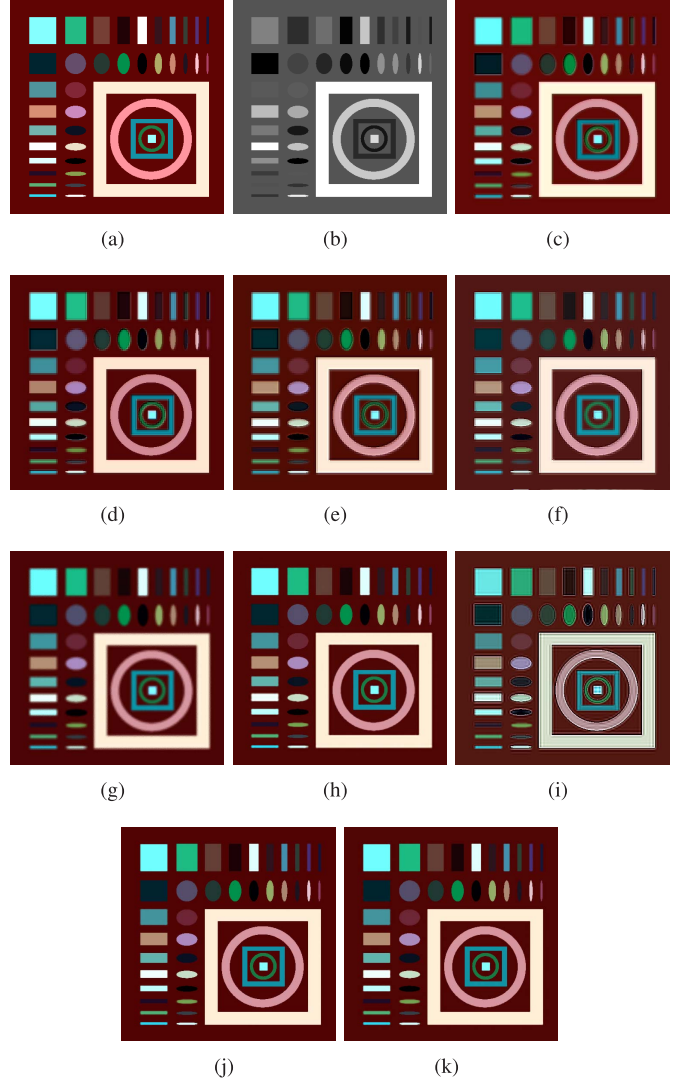


Fig. 4. Comparison of different pansharpening methods on Pattern image. The resulting image is represented as a true-color combination of the Red, Green and Blue bands. The scene presented is of size 500×500 . (a) Reference MS image. (b) Pan image. (c) FIHS-SA fused image [18]. (d) GSA fused image [20]. (e) AWLP fused image [23]. (f) GLP-CBD fused image [22]. (g) P+XS fused image [28]. (h) Fused image using TV_1 [30]. (i) Fused image using TV_2 [35]. (j) Fused image using the proposed method LR-TV. (k) Fused image using the proposed method PCP-TV.

B. Quality Assessment Indices

In order to evaluate the quality of the fused results of different methods, both visual inspection and quantitative assessment were conducted. Visual inspection can give a general idea of the image quality as perceived by human

TABLE VI
QUANTITATIVE EVALUATION OF THE FUSED RESULTS OF DIFFERENT METHODS ON THE PATTERN DATA

Pattern	Ideal	FIHS-SA	GSA	AWLP	GLP-CBD	P+XS	TV_1	TV_2	LR-TV	PCP-TV
Ave	Err_max	0	18.5	18.5	20.4	41.5	21.0	15.8	40.7	10.3
	Err_ℓ₁	0	1.16	0.831	0.926	0.757	1.30	0.394	2.59	0.0589
	Err_ℓ₂	0	1.91	1.84	2.40	2.03	2.70	0.944	4.25	0.269
	Q	1	0.775	0.831	0.760	0.830	0.750	0.895	0.646	0.908
SAM	0	3.76	3.13	3.21	2.46	3.77	0.790	5.47	0.221	0.319
ERGAS	0	5.33	5.36	6.50	5.53	7.16	2.51	9.65	0.798	1.17
Q4	1	0.820	0.764	0.808	0.843	0.763	0.898	0.744	0.910	0.908

observers, but it may be subjectively biased. Quantitative measures are attractive, because they are defined mathematically and independent of individual observers. Let $\hat{\mathbf{v}} = [\hat{\mathbf{v}}_1, \hat{\mathbf{v}}_2, \dots, \hat{\mathbf{v}}_L] \in \mathbb{R}^{N_1 \times N_2 \times L}$ be the high resolution reference MS image, where $\hat{\mathbf{v}}_l$ is the image of band l . Let $N = N_1 N_2$ be the total number of pixels in each band. In our experiments, we employ the following universal image quality indices for the evaluation of fused images. As the universal indices are proposed initially for monochrome images, we shall calculate these measurements for each band of the MS image and average the results over all the bands to obtain a global measure.

- (1) Error based measurements are the most widely used quality indices in image processing community, such as the maximum error,

$$\text{Err}_{\text{max}} = \max_{n_1, n_2} |\mathbf{v}_l[n_1, n_2] - \hat{\mathbf{v}}_l[n_1, n_2]|, \quad (36)$$

the ℓ_1 norm error

$$\text{Err}_{\ell_1} = \frac{1}{N} \sum_{n_1, n_2} |\mathbf{v}_l[n_1, n_2] - \hat{\mathbf{v}}_l[n_1, n_2]|, \quad (37)$$

and the ℓ_2 norm error

$$\text{Err}_{\ell_2} = \sqrt{\frac{1}{N} \sum_{n_1, n_2} (\mathbf{v}_l[n_1, n_2] - \hat{\mathbf{v}}_l[n_1, n_2])^2}. \quad (38)$$

- (2) The Q index proposed by Wang and Bovik [50] has shown great ability in measuring image distortions. It combines the loss of correlation, luminance distortion and contrast distortion of an image and is calculated by:

$$Q = \frac{4\sigma_{(\mathbf{v}_l, \hat{\mathbf{v}}_l)} \bar{\mathbf{v}}_l \bar{\hat{\mathbf{v}}}_l}{(\sigma_{\mathbf{v}_l}^2 + \sigma_{\hat{\mathbf{v}}_l}^2)[(\bar{\mathbf{v}}_l)^2 + (\bar{\hat{\mathbf{v}}}_l)^2]}, \quad (39)$$

where $\sigma_{(\mathbf{v}_l, \hat{\mathbf{v}}_l)}$ is the covariance between pixel values in the fused image and in the reference high resolution MS image, $\bar{\mathbf{v}}_l$ and $\bar{\hat{\mathbf{v}}}_l$ are the mean value of the fused image and of the reference image, respectively, and $\sigma_{\mathbf{v}_l}^2$ and $\sigma_{\hat{\mathbf{v}}_l}^2$ are the variance of the fused image and of the reference image, respectively.

In addition to the above universal measures, we also employ quality indices that have been specifically developed by the remote sensing community for evaluating the quality of pancharpened MS image, with much attention paid to the spectral and spatial quality. The following indices are considered.

- (3) The Spectral Angle Mapper (SAM) [51] reveals spectral distortion of the fused image by calculating the absolute

angle between the spectral vector of each pixel of the fused image and that of the reference image:

$$\text{SAM} = \arccos \left(\frac{\langle \mathbf{v}[n_1, n_2], \hat{\mathbf{v}}[n_1, n_2] \rangle}{\|\mathbf{v}[n_1, n_2]\|_2 \|\hat{\mathbf{v}}[n_1, n_2]\|_2} \right). \quad (40)$$

It is usually averaged over the whole image and a value equal to zero means that there is no spectral distortion.

- (4) The ERGAS index proposed by Ranchin and Wald is the French acronym for “Erreur Relative Globale Adimensionnelle de Synthèse” (relative dimensionless global error in synthesis) [52]. This index gives a global quality assessment of the fused MS image and is defined as

$$\text{ERGAS} = 100 \frac{d_h}{d_l} \sqrt{\frac{1}{L} \sum_{l=1}^L \left(\frac{\text{RMSE}(l)}{\mu(l)} \right)^2}, \quad (41)$$

where d_h and d_l are respectively the pixel sizes of the Pan and of the MS image, $\mu(l)$ is the mean of the l -th band of the reference image, and RMSE(l) is the root mean square error between the l -th band of the fused image and that of the reference image.

- (5) The quality index Q4 has been specifically developed for assessing MS images with four spectral bands [51]. It extends the idea of the universal Q index, which was initially designed for monochrome images, to the application on MS images based on the theory of hypercomplex numbers, or quaternions. The authors propose to represent an MS image of four bands by $\mathbf{z} = a + ib + jc + kd$ with i, j, k the imaginary units and a, b, c and d the radiance values of a pixel respectively in the Blue, Green, Red and Nir bands. With this new representation, the Q4 index can be calculated using the same equation (39) of the Q index. This index considers both spectral and spatial qualities of the fused image.

C. Fusion Results on Pattern Data

We start with the simulated Pattern dataset. Table V gives a brief description of the dataset. The test image is generated with different shapes by using pure pixels randomly selected from USGS spectral library,⁸ see Fig. 4(a).

In Fig. 4, we show the fusion results of different methods in form of true color images (as a combination of the Red, Green and Blue bands). The reference MS and Pan image at high resolution are also presented. Visually, it can be observed that

⁸ Available online at <http://speclab.cr.usgs.gov/spectral.lib06>.

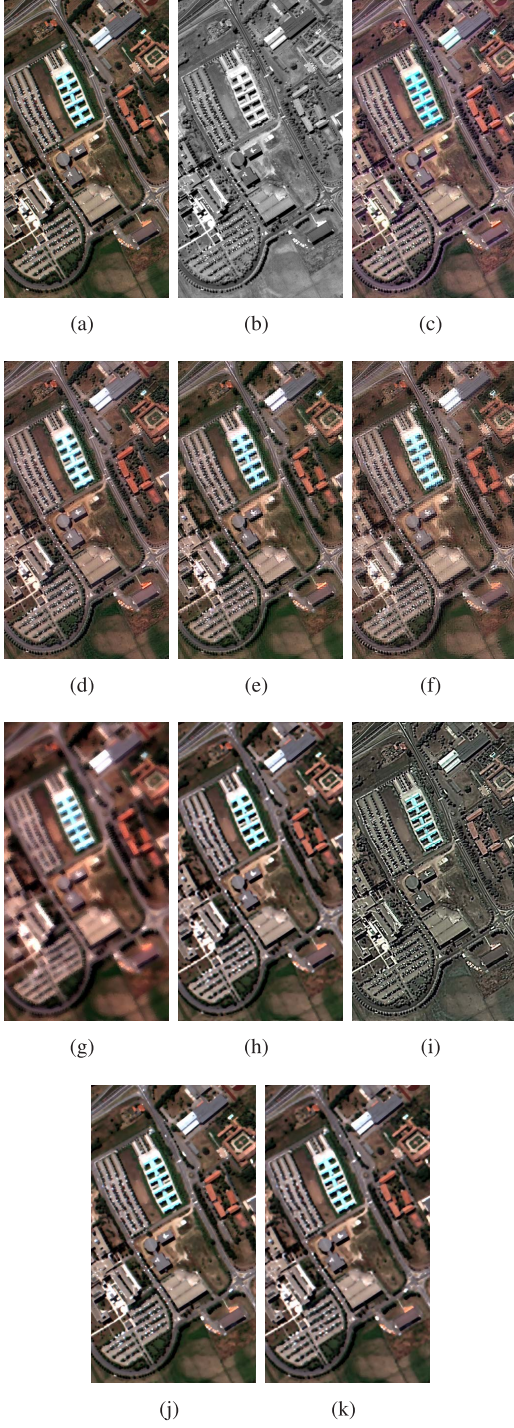


Fig. 5. Comparison of different pansharpening methods on Pavia image. The resulting image is represented as a true-color combination of the Red, Green and Blue bands. The scene presented is of size 608×336 , at 1.3-m resolution. (a) Reference MS image. (b) Pan image. (c) FIHS-SA fused image [18]. (d) GSA fused image [20]. (e) AWLP fused image [23]. (f) GLP-CBD fused image [22]. (g) P+XS fused image [28]. (h) Fused image using TV_1 [30]. (i) Fused image using TV_2 [35]. (j) Fused image using the proposed method LR-TV. (k) Fused image using the proposed method PCP-TV.

the two proposed methods LR-TV and PCP-TV (cf. Figs. 4(j) and 4(k)) have the best spectral quality. TV based method TV_1 provides also a good spectral quality. In contrast, TV_2 exhibits a high spectral distortion. Component substitution methods with spectral adjustment FIHS-SA and GSA produce

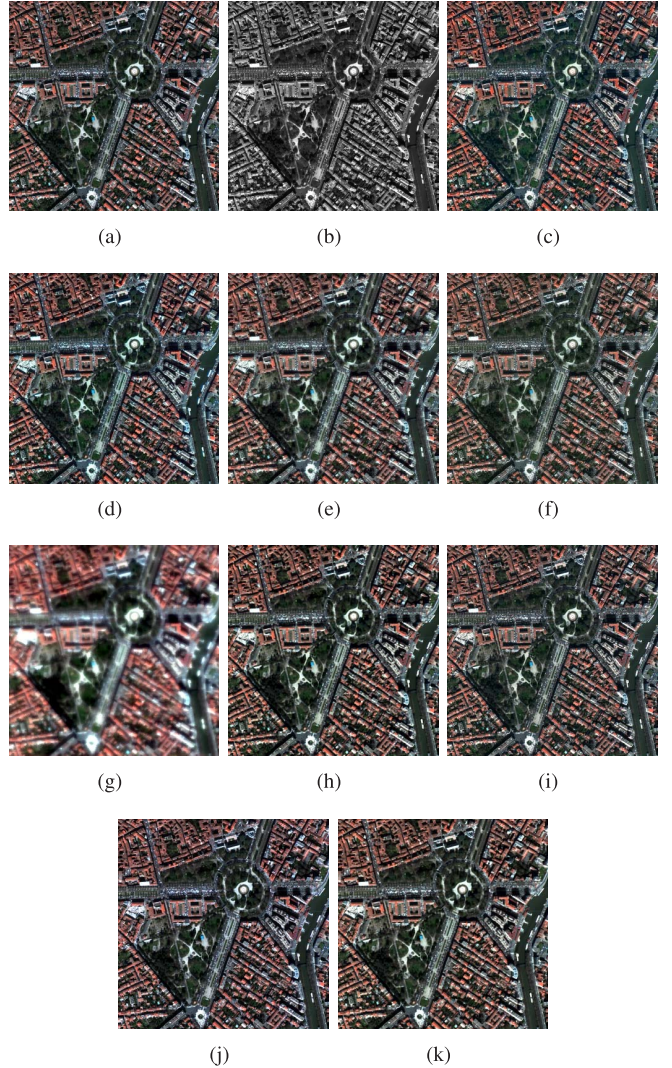


Fig. 6. Comparison of different pansharpening methods on Pléiades images. The resulting image is represented as a true-color combination of the Red, Green and Blue bands. The scene presented is of size 1024×1024 , at 0.8-m resolution. (a) Reference MS image. (b) Pan image. (c) FIHS-SA fused image [18]. (d) GSA fused image [20]. (e) AWLP fused image [23]. (f) GLP-CBD fused image [22]. (g) P+XS fused image [28]. (h) Fused image using TV_1 [30]. (i) Fused image using TV_2 [35]. (j) Fused image using the proposed method LR-TV. (k) Fused image using the proposed method PCP-TV.

fused images with spectral quality competitive to that of multiresolution-analysis methods AWLP and GLP-CBD. For the spatial quality, we observe that TV_2 performs the worst. Both FIHS-SA and P+XS result in a blurred fused image (Figs. 4(c) and 4(g)). GSA, AWLP and GLP-CBD suffer from ringing and aliasing artifacts on the rectangles and circles in the fused images (cf. Figs. 4(d), 4(e), and 4(f)).

In Table VI, we present a detailed quantitative evaluation of the fused results of different methods using all the aforementioned image quality indices (cf. Sect. V-B). The ideal value of each index is also given and the best results are highlighted in bold. We can see that, in accordance with the visual inspection, the two proposed methods LR-TV and PCP-TV perform significantly better than the other methods, with LR-TV performing slightly better than PCP-TV. The method

TABLE VII
DATA SET DESCRIPTION: ROSIS PAVIA DATA

Type	simulated from real HS: $(\mathbf{v}, \mathbf{p}) = \mathbf{A}^T \mathbf{s}$,
Size	$\mathbf{u}: 152 \times 84 \times 4$, $\mathbf{p}: 608 \times 336$
\mathbf{A}	IKONOS spectral responses
$\mathbf{s} \in \mathbb{R}^{103 \times 608 \times 336}$	ROSIS Pavia Image
\mathcal{R}	downsampling $S = 4$, PSF Gaussian (std. dev. $s_h = s_v = 1.93$)

TABLE VIII
QUANTITATIVE EVALUATION OF THE FUSED RESULTS OF DIFFERENT METHODS ON THE ROSIS PAVIA DATA

Pavia		Ideal	FIHS-SA	GSA	AWLP	GLP-CBD	P+XS	TV_1	TV_2	LR-TV	PCP-TV
Ave	Err_max	0	8.93	8.47	10.8	14.6	13.4	12.3	42.3	9.15	11.4
	Err_ell_1	0	0.395	0.363	0.397	0.445	0.573	0.301	2.49	0.249	0.284
	Err_ell_2	0	0.597	0.524	0.633	0.696	0.884	0.529	3.06	0.423	0.495
	Q	1	0.850	0.873	0.857	0.813	0.623	0.885	0.478	0.922	0.897
	SAM	0	6.33	5.35	6.55	6.12	6.16	3.50	14.4	3.48	3.49
	ERGAS	0	6.08	5.22	6.41	7.01	8.73	5.18	33.9	4.24	4.86
	Q4	1	0.871	0.887	0.880	0.825	0.622	0.885	0.562	0.925	0.898

TABLE IX
DATA SET DESCRIPTION: PLEIADES DATA

Type	\mathbf{v} real, (\mathbf{u}, \mathbf{p}) simulated
Size	$\mathbf{u}: 256 \times 256 \times 4$, $\mathbf{p}: 1024 \times 1024$
\mathcal{R}	downsampling $S = 4$, PSF - Estimated from \mathbf{u} and \mathbf{v}

TABLE X
QUANTITATIVE EVALUATION OF THE FUSED RESULTS OF DIFFERENT METHODS ON THE PLÉIADES DATA

Pléiades		Ideal	FIHS-SA	GSA	AWLP	GLP-CBD	P+XS	TV_1	TV_2	LR-TV	PCP-TV
Ave	Err_max	0	584.5	607.1	644.5	980.4	786.0	802.6	534.9	541.9	709.4
	Err_ell_1	0	25.3	25.8	22.2	21.8	38.0	21.3	16.9	15.6	19.9
	Err_ell_2	0	34.6	36.7	34.7	34.0	56.6	37.7	25.6	25.2	34.0
	Q	1	0.906	0.893	0.908	0.920	0.658	0.884	0.952	0.948	0.906
	SAM	0	5.13	5.56	4.82	4.57	5.98	3.51	3.91	3.70	3.55
	ERGAS	0	4.31	4.56	4.33	4.20	7.13	4.78	3.15	3.13	4.27
	Q4	1	0.880	0.852	0.895	0.896	0.661	0.886	0.943	0.934	0.902

TV_1 also shows a good performance whereas TV_2 performs the worst. Among non-variational methods, multiresolution-analysis method GLP-CBD presents a higher spectral quality (low SAM value) whereas component substitution method FIHS-SA has a better spatial quality (low ERGAS value).

D. Fusion Results on ROSIS Pavia Data

In this section, we present the experimental results on a subset of the ROSIS Pavia data (Fig. 5(a)). We generated a couple (\mathbf{v}, \mathbf{p}) according to Equation (9) using the spectral responses of the IKONOS sensor [53] and a hyperspectral image of the urban area of the University of Pavia, Italy, acquired by the Reflective Optics Imaging Spectrographic System (ROSIS) optical sensor. The image has a very high spatial resolution of 1.3 meters per pixel. The number of bands in the original acquired image is 103, covering the spectral range from 0.43 to 0.86 μm . The low resolution MS image was computed as $\mathbf{u} = \mathcal{R}\mathbf{v}$ using a downsampling factor $S = 4$ and a lowpass filter with symmetric Gaussian shape. The characteristics of the experimental setting are summarized in Tab. VII.

Fig. 5 illustrates the reference image and the fused results of different methods. This dataset is more difficult with many

cars in the scene. Through visual inspection, we can see that with this dataset, P+XS performs the worst and TV_2 has severe spectral distortion. The pansharpened images obtained by FIHS-SA and GSA have better spatial quality but FIHS-SA suffers from spectral distortion. In contrast, the weighted TV based methods (TV_1 and the two proposed methods) show better spectral quality. The fusion results of TV_1 and of the two proposed methods are visually quite similar. Spatial distortions, like aliasing artifact can be easily observed on the fused images obtained by AWLP and GLP-CBD (Figs. 5(e) and 5(f)). Table VIII reports the quantitative evaluation of the fused results of different methods using universal and specific image quality indices. We can see that TV_2 has the worst results. On average, GSA has the lowest maximum error. PCP-TV and LR-TV perform the best in terms of all the other indices. Again the two proposed methods show comparable results, with LR-TV performing slightly better than PCP-TV.

E. Fusion Results on Pléiades Data

The Pléiades images provided by the French Space Agency CNES (Centre National d'Études Spatiales) were taken over the city of Toulouse in France. The dataset consists of MS images with four bands (Blue, Green, Red and Nir) at both

high resolution of 0.8-m and low resolution of 3.2-m. The Pan image of the same scene at 0.8-m resolution is also provided. In particular, the Pan image in this dataset is generated as the average of the red and green bands of the high resolution MS image; that is, the linear coefficient vector α is given by $\alpha = (0, 0.5, 0.5, 0)$. The main advantage of the Pléiades dataset is that the reference high resolution MS image is available. So, we can evaluate the fusion results of different pansharpening methods with all the aforementioned quality indices directly. The Pan image and the low resolution MS image used in our experiments are respectively of size 1024×1024 and 256×256 , while the reference high resolution MS image is of size 1024×1024 . A brief description of the dataset can be found in Table IX.

In Fig. 6 we show the fusion results of different methods in form of true color images (as a combination of the Red, Green and Blue bands). We can see that only the variational method P+XS suffers from both severe spectral and spatial distortion (cf. Fig. 6(g)). The results produced by the other methods are visually very similar. In Table X, we list the quantitative assessment results of different methods using universal and specific image quality indices. We can see that TV_2 and LR-TV outperform the other methods in terms of the universal indices (Err_max, Err_ℓ₁, Err_ℓ₂ and Q). On average, TV_2 performs the best in terms of Err_max and Q index and LR-TV performs the best in terms of Err_ℓ₁ and Err_ℓ₂. Concerning the specific image quality indices, TV_1 has the best spectral quality (lowest SAM value). TV_2 performs the best in terms of Q4 index and LR-TV has the lowest ERGAS value. Remarkably, the TV_2 performs clearly better on this dataset than on other datasets. This may be due to the fact that the linear coefficient vector for the Pléiades dataset is known ($\mathbf{M}_2 = \alpha$) whereas without *a priori* information we set $\mathbf{M}_2 = \{\frac{1}{4}\mathbf{I}, \frac{1}{4}\mathbf{I}, \frac{1}{4}\mathbf{I}, \frac{1}{4}\mathbf{I}\}$ for the other datasets. This again proves that the estimation of the exact value of α has an important effect on the pansharpening process.

VI. CONCLUSION

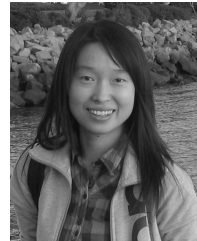
In this paper, a new variational pansharpening model is presented. With the objective that the fused image should preserve both low-rank structure of the MS image and important geometric information of the Pan image, two pansharpening inference criteria, named LR-TV and PCP-TV respectively, are introduced. Both methods employ a weighted version of the total variation norm for preserving edge locations. In order to exploit the low-rank structure, LR-TV estimates the underlying linear coefficients between the Pan image and the fused image by linear regression while PCP-TV resorts to the principal component pursuit. The optimization problems can be efficiently solved within the framework of proximal splitting methods for convex optimization, with the proposed PanSALSA algorithm. The main difference between the proposed methods and other pansharpening methods is that, instead of the tight linear relationship assumption between the Pan image and the fused high resolution image, we investigate the low-rank structure of the data matrix composed of the fused image and an extra band of the Pan image.

Experimental results show that both LR-TV and PCP-TV outperform traditional methods in terms of both subjective assessment via visual inspection and objective quantitative assessment. In our method, we select the optimum value of the regularization parameters among a group of preset values. We have introduced the selection method based on the V-curve, which, in the reported experiments, yielded nearly optimum results. Improvements may be obtained by further analysis of the relationship between different regularization terms in the optimization problems.

REFERENCES

- [1] E. L. Waltz, "Data fusion for C³I: A tutorial," in *Command, Control, Communications Intelligence (C³I) Handbook*. Palo Alto, CA, USA: EW Communications, Inc., 1986, pp. 217–226.
- [2] R. R. Colditz *et al.*, "Influence of image fusion approaches on classification accuracy: A case study," *Int. J. Remote Sens.*, vol. 27, no. 15, pp. 3311–3335, 2006.
- [3] C. Thomas, T. Ranchin, L. Wald, and J. Chanussot, "Synthesis of multispectral images to high spatial resolution: A critical review of fusion methods based on remote sensing physics," *IEEE Trans. Geosci. Remote Sens.*, vol. 46, no. 5, pp. 1301–1312, May 2008.
- [4] M. M. Khan, J. Chanussot, and L. Alparone, "Pansharpening of hyperspectral images using spatial distortion optimization," in *Proc. 16th IEEE Int. Conf. Image Process. (ICIP)*, Cairo, Egypt, Nov. 2009, pp. 2853–2856.
- [5] B. Luo, M. M. Khan, T. Bienvenu, and J. Chanussot, "Pansharpening with a decision fusion based on the local size information," in *Proc. 17th IEEE Int. Conf. Image Process. (ICIP)*, Hong Kong, China, Sep. 2010, pp. 1977–1980.
- [6] I. Amro, J. Mateos, and M. Vega, "Bayesian super-resolution pansharpening using contourlets," in *Proc. 17th IEEE Int. Conf. Image Process. (ICIP)*, Hong Kong, China, Sep. 2010, pp. 809–812.
- [7] I. Amro, J. Mateos, and M. Vega, "Parameter estimation in Bayesian super-resolution pansharpening using contourlets," in *Proc. 18th IEEE Int. Conf. Image Process. (ICIP)*, Brussels, Belgium, Sep. 2011, pp. 1345–1348.
- [8] M. Vega, J. Mateos, R. Molina, and A. K. Katsaggelos, "Super resolution of multispectral images using ℓ₁ image models and interband correlations," *J. Signal Process. Syst.*, vol. 65, no. 3, pp. 509–523, 2011.
- [9] S. Baronti, B. Aiazzi, M. Selva, A. Garzelli, and L. Alparone, "A theoretical analysis of the effects of aliasing and misregistration on pansharpened imagery," *IEEE J. Sel. Topics Signal Process.*, vol. 5, no. 3, pp. 446–453, Jun. 2011.
- [10] G. A. Licciardi, M. M. Khan, and J. Chanussot, "Fusion of hyperspectral and panchromatic images: A hybrid use of indusion and nonlinear PCA," in *Proc. 19th IEEE Int. Conf. Image Process. (ICIP)*, Orlando, FL, USA, Sep./Oct. 2012, pp. 2133–2136.
- [11] P. Sirguey, R. Mathieu, Y. Arnaud, M. M. Khan, and J. Chanussot, "Improving MODIS spatial resolution for snow mapping using wavelet fusion and ARSIS concept," *IEEE Geosci. Remote Sens. Lett.*, vol. 5, no. 1, pp. 78–82, Jan. 2008.
- [12] F. Bovolo, L. Bruzzone, L. Capobianco, A. Garzelli, S. Marchesi, and F. Nencini, "Analysis of the effects of pansharpening in change detection on VHR images," *IEEE Geosci. Remote Sens. Lett.*, vol. 7, no. 1, pp. 53–57, Jan. 2010.
- [13] L. Alparone, L. Wald, J. Chanussot, C. Thomas, P. Gamba, and L. M. Bruce, "Comparison of pansharpening algorithms: Outcome of the 2006 GRS-S data-fusion contest," *IEEE Trans. Geosci. Remote Sens.*, vol. 45, no. 10, pp. 3012–3021, Oct. 2007.
- [14] R. Welch and W. Ahlers, "Merging multiresolution SPOT HRV and landsat TM data," *Photogramm. Eng. Remote Sens.*, vol. 53, no. 3, pp. 301–303, 1987.
- [15] C. Laben and B. Brower, "Process for enhancing the spatial resolution of multispectral imagery using pan-sharpening," Patent U.S. 6011875, Jan. 4, 2000.
- [16] V. P. Shah, N. H. Younan, and R. L. King, "An efficient pan-sharpening method via a combined adaptive PCA approach and contourlets," *IEEE Trans. Geosci. Remote Sens.*, vol. 46, no. 5, pp. 1323–1335, May 2008.
- [17] T.-M. Tu, S.-C. Su, H.-C. Shyu, and P. S. Huang, "A new look at IHS-like image fusion methods," *Inform. Fusion*, vol. 2, no. 3, pp. 177–186, 2001.

- [18] T.-M. Tu, P. S. Huang, C.-L. Hung, and C.-P. Chang, "A fast intensity-hue-saturation fusion technique with spectral adjustment for IKONOS imagery," *IEEE Geosci. Remote Sens. Lett.*, vol. 1, no. 4, pp. 309–312, Oct. 2004.
- [19] M. Choi, "A new intensity-hue-saturation fusion approach to image fusion with a tradeoff parameter," *IEEE Trans. Geosci. Remote Sens.*, vol. 44, no. 6, pp. 1672–1682, Jun. 2006.
- [20] B. Aiazzi, S. Baronti, and M. Selva, "Improving component substitution pansharpening through multivariate regression of MS +Pan data," *IEEE Trans. Geosci. Remote Sens.*, vol. 45, no. 10, pp. 3230–3239, Oct. 2007.
- [21] J. Núñez, X. Otazu, O. Fors, A. Prades, V. Palà, and R. Arbiol, "Multiresolution-based image fusion with additive wavelet decomposition," *IEEE Trans. Geosci. Remote Sens.*, vol. 37, no. 3, pp. 1204–1211, May 1999.
- [22] B. Aiazzi, L. Alparone, S. Baronti, and A. Garzelli, "Context-driven fusion of high spatial and spectral resolution images based on oversampled multiresolution analysis," *IEEE Trans. Geosci. Remote Sens.*, vol. 40, no. 10, pp. 2300–2312, Oct. 2002.
- [23] X. Otazu, M. González-Audicana, O. Fors, and J. Núñez, "Introduction of sensor spectral response into image fusion methods. Application to wavelet-based methods," *IEEE Trans. Geosci. Remote Sens.*, vol. 43, no. 10, pp. 2376–2385, Oct. 2005.
- [24] T. Ranchin and L. Wald, "The wavelet transform for the analysis of remotely sensed images," *Int. J. Remote Sens.*, vol. 14, no. 3, pp. 615–619, 1993.
- [25] D. A. Yocky, "Multiresolution wavelet decomposition image merger of landsat thematic mapper and SPOT panchromatic data," *Photogrammetric Eng. Remote Sens.*, vol. 62, no. 9, pp. 1067–1074, 1996.
- [26] B. Garguet-Duport, J. Girel, J.-M. Chassery, and G. Pautou, "The use of multiresolution analysis and wavelets transform for merging SPOT panchromatic and multispectral image data," *Photogrammetric Eng. Remote Sens.*, vol. 62, no. 9, pp. 1057–1066, 1996.
- [27] V. Karathanassi and S. Ioannidou, "Investigation of the dual-tree complex and shift-invariant discrete wavelet transforms on Quickbird image fusion," *IEEE Geosci. Remote Sens. Lett.*, vol. 4, no. 1, pp. 16–170, Jan. 2007.
- [28] C. Ballester, V. Caselles, L. Igual, J. Verdera, and B. Rougé, "A variational model for P+XS image fusion," *Int. J. Comput. Vis.*, vol. 69, no. 1, pp. 43–58, 2006.
- [29] M. Möller, T. Wittman, and A. L. Bertozzi, "A variational approach to hyperspectral image fusion," *Proc. SPIE*, vol. 7334, pp. 73341E.1–73341E.10, Apr. 2009.
- [30] X. He, L. Condat, J. Chanussot, and J. Xia, "Pansharpening using total variation regularization," in *Proc. IEEE Int. Geosci. Remote Sens. Symp. (IGARSS)*, Munich, Germany, Jul. 2012, pp. 166–169.
- [31] L. Rudin, S. Osher, and E. Fatemi, "Nonlinear total variation based noise removal algorithms," *Phys. D, Nonlinear Phenomena*, vol. 60, nos. 1–4, pp. 259–268, 1992.
- [32] X. Bresson and T. F. Chan, "Fast dual minimization of the vectorial total variation norm and applications to color image processing," *Inverse Problems Imag.*, vol. 2, no. 4, pp. 455–484, 2008.
- [33] Q. Yuan, L. Zhang, and H. Shen, "Hyperspectral image denoising employing a spectral-spatial adaptive total variation model," *IEEE Trans. Geosci. Remote Sens.*, vol. 50, no. 10, pp. 3660–3677, Oct. 2012.
- [34] A. Chambolle and T. Pock, "A first-order primal-dual algorithm for convex problems with applications to imaging," *J. Math. Imag. Vis.*, vol. 40, no. 1, pp. 120–145, 2011.
- [35] F. Palsson, J. R. Sveinsson, M. O. Ulfarsson, and J. A. Benediktsson, "A new pansharpening method using an explicit image formation model regularized via total variation," in *Proc. Int. Geosci. Remote Sens. Symp. (IGARSS)*, Munich, Germany, Jul. 2012, pp. 2288–2291.
- [36] E. J. Candès, X. Li, Y. Ma, and J. Wright, "Robust principal component analysis?" *J. ACM*, vol. 58, no. 3, pp. 11:1–11:37, 2011.
- [37] E. J. Candès and Y. Plan, "Tight oracle inequalities for low-rank matrix recovery from a minimal number of noisy random measurements," *IEEE Trans. Inf. Theory*, vol. 57, no. 4, pp. 2342–2359, Apr. 2011.
- [38] V. Chandrasekaran, S. Sanghavi, P. A. Parrilo, and A. S. Willsky, "Rank-sparsity incoherence for matrix decomposition," *SIAM J. Optim.*, vol. 21, no. 2, pp. 572–596, 2011.
- [39] M. Golbabaei and P. Vandergheynst, "Hyperspectral image compressed sensing via low-rank and joint-sparse matrix recovery," in *Proc. IEEE Int. Conf. Acoust., Speech, Signal Process. (ICASSP)*, Kyoto, Japan, Mar. 2012, pp. 2741–2744.
- [40] M. Golbabaei and P. Vandergheynst, "Joint trace/TV norm minimization: A new efficient approach for spectral compressive imaging," in *Proc. IEEE Int. Conf. Image Process. (ICIP)*, Orlando, FL, USA, Sep./Oct. 2012, pp. 933–936.
- [41] M. V. Afonso, J. M. Bioucas-Dias, and M. A. T. Figueiredo, "An augmented Lagrangian approach to the constrained optimization formulation of imaging inverse problems," *IEEE Trans. Image Process.*, vol. 20, no. 3, pp. 681–695, Mar. 2011.
- [42] J. Eckstein and D. P. Bertsekas, "On the Douglas–Rachford splitting method and the proximal point algorithm for maximal monotone operators," *Math. Program.*, vol. 55, nos. 1–3, pp. 293–318, 1992.
- [43] D. Gabay and B. Mercier, "A dual algorithm for the solution of nonlinear variational problems via finite element approximation," *Comput. Math. Appl.*, vol. 2, no. 1, pp. 17–40, 1976.
- [44] R. Glowinski and A. Marroco, "Sur l'approximation, par éléments finis d'ordre un, et la résolution, par pénalisation-dualité d'une classe de problèmes de Dirichlet non linéaires," *Revue Française d'Autom., Inform. Recherche Oper.*, vol. 9, no. R2, pp. 41–76, 1975.
- [45] P. Combettes and J.-C. Pesquet, "Proximal splitting methods in signal processing," in *Fixed-Point Algorithms for Inverse Problems in Science and Engineering*. New York, NY, USA: Springer-Verlag, 2011, pp. 185–212.
- [46] J.-B. Urruty and C. Lemaréchal, *Fundamentals of Convex Analysis*. New York, NY, USA: Springer-Verlag, 2001.
- [47] S. Boyd, N. Parikh, E. Chu, B. Peleato, and J. Eckstein, "Distributed optimization and statistical learning via the alternating direction method of multipliers," *Found. Trends Mach. Learn.*, vol. 3, no. 1, pp. 1–122, 2011.
- [48] G. Vivone, "Multispectral and hyperspectral pansharpening: A critical examination and new developments," Ph.D. dissertation, Dept. Inf. Eng., Electr. Eng. Appl. Math., Univ. Salerno, Fisciano, Italy, Mar. 2014.
- [49] B. Aiazzi, L. Alparone, S. Baronti, A. Garzelli, and M. Selva, "MTF-tailored multiscale fusion of high-resolution MS and pan imagery," *Photogrammetric Eng. Remote Sens.*, vol. 72, no. 5, pp. 591–596, 2006.
- [50] Z. Wang and A. C. Bovik, "A universal image quality index," *IEEE Signal Process. Lett.*, vol. 9, no. 3, pp. 81–84, Mar. 2002.
- [51] L. Alparone, S. Baronti, A. Garzelli, and F. Nencini, "A global quality measurement of pan-sharpened multispectral imagery," *IEEE Geosci. Remote Sens. Lett.*, vol. 1, no. 4, pp. 313–317, Oct. 2004.
- [52] T. Ranchin and L. Wald, "Fusion of high spatial and spectral resolution images: The ARSIS concept and its implementation," *Photogrammetric Eng. Remote Sens.*, vol. 66, no. 1, pp. 49–61, 2000.
- [53] J. Grodecki and G. Dial, "IKONOS geometric accuracy," in *Proc. Joint Workshop ISPRS Working Groups I/2, I/5 IV/7 High Resolution Mapping Space*, Sep. 2001, pp. 19–21.



Xiyan He received the Generalist Engineer degree from École Centrale Paris, Paris, France, in 2006, the M.E. degree in pattern recognition and intelligent system from Xi'an Jiaotong University, Xi'an, China, and the Ph.D. degree in computer science from the University of Technology of Troyes, Troyes, France, in 2009. She was a Teaching Assistant with the University of Technology of Troyes in 2009, a Post-Doctoral Research Fellow with the Research Centre for Automatic Control of Nancy, Nancy, France, in 2010, and a Teaching Assistant with the University of Pierre-Mendès-France, Grenoble, France, in 2011. Since 2012, she has been a Post-Doctoral Research Fellow with the Grenoble Laboratory of Image, Speech, Signal and Automatics, Grenoble. Her main research interests include machine learning, pattern recognition, and data fusion, with special focus on applications to remote sensed images.



Laurent Condat received the M.S. degree in computer science from the École Nationale Supérieure d'Informatique et de Mathématiques Appliquées de Grenoble, Grenoble, France, and the M.S. and Ph.D. degrees in applied mathematics from Joseph Fourier University, Grenoble, and the Institut National Polytechnique de Grenoble (INPG), Grenoble, in 2003 and 2006, respectively. From 2006 to 2008, he held a post-doctoral position with the Helmholtz Zentrum München, Munich, Germany. Since 2008, he has been a Permanent CNRS Research Fellow. He was

with the GREYC Laboratory, Caen, France, from 2008 to 2012, and he has been with the Grenoble Images Speech Signals and Automatics Laboratory, Grenoble, since 2012.

His area of interests include sampling and inverse problems in signal and image processing.

Dr. Condat was a recipient of the Best Student Paper Award at the IEEE International Conference on Image Processing in 2005 and the Best Ph.D. Award from the INPG in 2007.



Jocelyn Chanussot (M'04–SM'04–F'12) received the M.Sc. degree in electrical engineering from the Grenoble Institute of Technology (Grenoble INP), Grenoble, France, in 1995, and the Ph.D. degree from Savoie University, Annecy, France, in 1998. In 1999, he was with the Geography Imagery Perception Laboratory for the Delegation Générale de l'Armement (DGA - French National Defense Department). Since 1999, he has been with Grenoble INP, where he was an Assistant Professor from 1999 to 2005, an Associate Professor from 2005 to 2007, and is currently a Professor of Signal and Image Processing. He is conducting his research with the Grenoble Images Speech Signals and Automatics Laboratory, Grenoble. His research interests include image analysis, multicomponent image processing, nonlinear filtering, and data fusion in remote sensing. He is a member of the Institut Universitaire de France (2012–2017). Since 2013, he has been an Adjunct Professor with the University of Iceland, Reykjavik, Iceland.

Dr. Chanussot was the Founding President of the IEEE Geoscience and Remote Sensing French Chapter (2007–2010), which received the 2010 IEEE GRSS-S Chapter Excellence Award. He was a co-recipient of the NORSIG 2006 Best Student Paper Award, the IEEE GRSS 2011 Symposium Best Paper Award, the IEEE GRSS 2012 Transactions Prize Paper Award, and the IEEE GRSS 2013 Highest Impact Paper Award. He was a member of the IEEE Geoscience and Remote Sensing Society AdCom (2009–2010), in charge of membership development. He was the General Chair of the first IEEE GRSS Workshop on Hyperspectral Image and Signal Processing: Evolution in Remote Sensing. He was the Chair (2009–2011) and Co-Chair of the GRS Data Fusion Technical Committee (2005–2008). He was a member of the Machine Learning for Signal Processing Technical Committee of the IEEE Signal Processing Society (2006–2008) and the Program Chair of the IEEE International Workshop on Machine Learning for Signal Processing, (2009). He was an Associate Editor of the IEEE GEOSCIENCE AND REMOTE SENSING LETTERS (2005–2007) and for *Pattern Recognition* (2006–2008). Since 2007, he has been an Associate Editor of the IEEE TRANSACTIONS ON GEOSCIENCE AND REMOTE SENSING. Since 2011, he has been the Editor-in-Chief of the IEEE JOURNAL OF SELECTED TOPICS IN APPLIED EARTH OBSERVATIONS AND REMOTE SENSING. In 2013, he was the Guest Editor for the PROCEEDINGS OF THE IEEE and the IEEE SIGNAL PROCESSING MAGAZINE in 2014. He is a member of the Institut Universitaire de France (2012–2017).



José M. Bioucas-Dias (S'87–M'95) received the E.E., M.Sc., Ph.D., and Agregado degrees in electrical and computer engineering from the Instituto Superior Técnico (IST), Engineering School, Technical University of Lisbon, Portugal, in 1985, 1991, 1995, and 2007, respectively.

He has been with the Department of Electrical and Computer Engineering, IST, since 1995, where he was an Assistant Professor from 1995 to 2007, and has been an Associate Professor since 2007. Since 1993, he has also been a Senior Researcher with the Pattern and Image Analysis Group, Instituto de telecomunicações, which is a private nonprofit research institution. His research interests include inverse problems, signal and image processing, pattern recognition, optimization, and remote sensing. He has authored and co-authored more than 230 scientific publications, including more than 60 journal papers (48 of them published in the IEEE journals), and 170 peer-reviewed international conference papers and book chapters.

Dr. Bioucas-Dias was an Associate Editor of the IEEE TRANSACTIONS ON CIRCUITS AND SYSTEMS (1997–2000), and is an Associate Editor of the IEEE TRANSACTIONS ON IMAGE PROCESSING and the IEEE TRANSACTIONS ON GEOSCIENCE AND REMOTE SENSING. He was a Guest Editor of the IEEE TRANSACTIONS ON GEOSCIENCE AND REMOTE SENSING for the *Special Issue on Spectral Unmixing of Remotely Sensed Data*, the IEEE JOURNAL OF SELECTED TOPICS IN APPLIED EARTH OBSERVATIONS AND REMOTE SENSING for the *Special Issue on Hyperspectral Image and Signal Processing*, and the IEEE SIGNAL PROCESSING MAGAZINE for the *Special Issue on Signal and Image Processing in Hyperspectral Remote Sensing*. He was the General Co-Chair of the 3rd IEEE GRSS Workshop on Hyperspectral Image and Signal Processing: Evolution in Remote Sensing (2011), and has been a member of program/technical committees of several international conferences.



Junshi Xia (S'11) received the B.S. degree in geographic information systems and the Ph.D. degree in photogrammetry and remote sensing from the China University of Mining and Technology, Beijing, China, in 2008 and 2013, respectively. He is currently pursuing the Ph.D. degree in image processing with the Grenoble Images Speech Signals and Automatics Laboratory, Grenoble Institute of Technology, Grenoble, France. His research interests include multiple classifier system in remote sensing, hyperspectral remote sensing image processing, and urban remote sensing.